



HAL
open science

Permeability and voids influence on the thermal signal, as inferred by multitemporal UAV-based infrared and visible images

Raphaël Antoine, Cyrille Fauchard, Jean-François Oehler, Philippe Joignant

► **To cite this version:**

Raphaël Antoine, Cyrille Fauchard, Jean-François Oehler, Philippe Joignant. Permeability and voids influence on the thermal signal, as inferred by multitemporal UAV-based infrared and visible images. *Journal of Hydrology*, 2020, 587, pp.124907. 10.1016/j.jhydrol.2020.124907 . hal-02864263

HAL Id: hal-02864263

<https://hal.science/hal-02864263>

Submitted on 10 Jun 2020

HAL is a multi-disciplinary open access archive for the deposit and dissemination of scientific research documents, whether they are published or not. The documents may come from teaching and research institutions in France or abroad, or from public or private research centers.

L'archive ouverte pluridisciplinaire **HAL**, est destinée au dépôt et à la diffusion de documents scientifiques de niveau recherche, publiés ou non, émanant des établissements d'enseignement et de recherche français ou étrangers, des laboratoires publics ou privés.

Permeability and voids influence on the thermal signal, as inferred by multitemporal UAV-based infrared and visible images [☆]

Raphael Antoine^{a,*}, Cyrille Fauchard^a, Jean-Francois Oehler^b, Philippe Joignant^c

*^aENDSUM Research Team, Centre d'Etudes et d'Expertise sur les Risques
l'Environnement, l'Aménagement et la Mobilité (CEREMA), 10, chemin de la
Poudrière, 76140 Le Grand Quevilly, France*

*^bService Hydrographique et océanographique de la Marine (SHOM), CS 92803 29228
BREST CEDEX 2*

^cGrand Port Maritime du Havre (GPMH), Terre-plein de la Barre, 76600 Le Havre

Abstract

This work presents for the first time associated thermal anomalies and deformations over subsurface cavities/voids located within two harbour quays in Le Havre Harbour, Normandy, France. An U.A.V. (Unmanned Aerial Vehicle) was used to acquire visible and thermal images over a diurnal cycle (from 7 a.m. to 5 p.m.). The visible images were processed to realize an altimetric model of the platforms by mean of the photogrammetric method, while the thermal infrared (TIR) images were used to study the evolution of their surface temperatures. The obtained 3D model shows the location of five topographic depressions on both quays. The analysis of the evolution of the

*Corresponding author

URL:

<https://www.cerema.fr/fr/innovation-recherche/recherche/equipes/endsum-evaluation-non-destructive>
(Raphael Antoine)

surface thermal field leads to the detection of cold thermal anomalies that are 1) not correlated to surface properties, and 2) spatially associated to the flanks of the five topographic depressions. Using a 2D conductive-radiative model, we show that these anomalies are not directly due to the thermally insulating effect of an air-filled area. Finally, we conclude that preferential infiltration and subsequent evaporation in the micro-fracturation present within the flanks of the depressions may be responsible for the strong cooling of these zones.

Keywords: , Remote Sensing, Thermal infrared, Photogrammetry, infiltration, Subsurface cavity, natural hazards, UAV

1. Introduction

Subsurface cavities/voids are important safety and economical issues for land-use planning. In this context, the identification/characterization of these objects remains an important challenge for stakeholders as well as for scientists. Recently, in situ measurements techniques made important progress to detect anthropic or natural subsurface cavities (Kaufmann et al. (2011), Vadillo et al. (2012), Kaufmann & Romanov (2016), Benavente et al. (2017), Kolesnikov & Fedin (2018), Vargemezis et al. (2019), Rahnema et al. (2020)). For instance, Artugyan et al. (2020) combined Ground Penetrating Radar (GPR) and Electrical Resistivity Imagery (ERI) to detect and characterize a karst massif in Romania (rock stratification and orientation, sections of these caves galleries and level of karstification). Martnez-Moreno et al. (2018) located a cave in Mira de Aire-Santo Antonio Range (Portugal) using

14 micro-gravity and ERI 3D-inversions. De Giorgi & Leucci (2014) imaged
15 shallow subsurface structures, including karstic features below a road in the
16 Salento Peninsula (Apulia region - South Italy), carrying out a Seismic Re-
17 fraction Tomography and GPR survey. Integrated interpretation led to the
18 delineation of hazard zone rich with karstic features and cavities. Mochales
19 et al. (2008) proposed a methodology based on the sequential application of
20 magnetic, GPR and microgravity techniques to detect underground cavities
21 and dolines. Cardarelli et al. (2009) used the joint interpretation of ERI
22 and seismic refraction tomography to map artificial cavities in the city of
23 Rome. Finally, in situ soil temperature sensors were also deployed to de-
24 tect subsurface cavities. Interestingly, Mosciki (2006) shown that thermal
25 anomalies associated to underground cavities can reach up to 1°C from field
26 measurements and numerical modelling. Although in situ measurements are
27 very useful on a local scale, they remain difficult to implement on important
28 surfaces and thus are economically unviable.

29 Remote sensing have also adressed the problem of subsurface cavities for
30 many years, using aerial or satellite observations (Ruth & Degner (1963),Pe-
31 ters et al. (1996),Youssef et al. (2012), Lee et al. (2016), Kim et al. (2019),
32 Jeffery et al. (2020)). For instance, Youssef et al. (2020) integrated remote
33 sensing (LANDSAT imagery) with ERI to characterize the role of agricul-
34 ture in the formation of sinkholes in Saudi Arabia. Chang & Hanssen (2014)
35 characterized the deformations associated to the upward migration of under-
36 ground cavities under the city of Heerlen (The Netherlands), using satellite
37 radar interferometry. Edmonds et al. (1987) demonstrated the potentialies

38 of detection of collapse and subsidence features in chalk and other limestone
39 rocks with an airborne multispectral scanner and thermal infrared (TIR)
40 data. This last method allows to map the surface temperatures of a soil
41 using a camera. Several teams in the world have shown the importance of
42 TIR method to map geological structures (Watson (1975), Sabins (2007),
43 Nasipuri et al. (2005)), hydrothermal systems (Antoine et al. (2009), Gaudin
44 et al. (2013)), to characterize water resources in arid zones (Leblanc et al.
45 (2007), Lopez et al. (2016)) or to detect underground burning coal (Vaster-
46 ling & Meyer (2013)). Campbell et al. (1996) used airborne TIR method to
47 locate hydrological features in karst watersheds. Gunn et al. (2008) detected
48 abandoned mineshafts in former mining areas after a TIR survey in Great
49 Britain. To our knowledge, although several studies have assessed the po-
50 tentiality of the TIR method for the characterization of subsurface cavities
51 (Rinker (1975), Wynne et al. (2008), Lee et al. (2016)), few is known about the
52 origin of the observed thermal anomalies, especially when slight subsidence
53 is observed. As a consequence, the methodology to adopt to detect these
54 objects before a collapse event remains unclear. In 2014, a TIR and visible
55 survey was performed above two parts of the Joannes Couvert platform (Le
56 Havre Harbour), the West and East Quays (hereafter named as WQ and
57 EQ), respectively. These structures were selected because of the continuous
58 formation of subsurface voids. For each area, the observations were acquired
59 with an UAV during a semi-diurnal cycle, allowing the TIR monitoring of
60 the surface temperatures (from sunrise to late afternoon) and the acquisition
61 of visible images. After a presentation of the geotechnical context and the

62 methodology used for this survey, the surface temperatures and the altimet-
63 ric map obtained by photogrammetry are shown for the WQ and EQ. Cold
64 areas associated to surface deformations are detected on both quays, with
65 a temperature contrast of 2-4°C compared to the surrounding environment.
66 The effect of the surface properties (thermal inertia, albedo) on the thermal
67 signal are first investigated, as they represent the main factors affecting the
68 surface temperatures of the soil. Then, a simplified 2D conductive-radiative
69 model of heat transfer is developped within one quay, namely the EQ, in
70 order to evaluate the direct thermal influence of a subsurface cavity on the
71 surface temperatures. Finally, the last section is dedicated to the analysis of
72 the role of potential fluid flow on the measured signal accross the deformed
73 quays.

74 **2. Geotechnical context**

75 Le Havre harbour is built in the Northern part of the estuary of the
76 Seine river (in Le Havre city, Normandy) and is essentially composed of
77 heterogeneous materials resulting from the World War 2 bombing. The study
78 sites (the West and East quays, hereafter named the WQ and EQ) are located
79 at the center of the harbour and is part of the Joannes Couvert quay (figure
80 1). This kilometric-size platform was part of the famous Transatlantic Cruise
81 Terminal in the 1930s. The building plan of the quays is known and in
82 particular, the backfills are massively composed of the war debris (stones and
83 fines materials). Over the years, the infiltration of salted water (associated
84 to storms and tides) within the structure lead to the withdrawal of the fine

85 particules from the quays and generated the formation of subsurface cavities,
86 as well as local surface subsidences (figure 2).

87 The figure 3 shows the structure of the WQ and the EQ, respectively.
88 The WQ is mainly composed of concrete backfill, a concrete slab and backfill
89 between 0 m and 9.50 m. Interestingly, the internal structure of the EQ is
90 very different, and essentially constituted of :

- 91 • Limestone masonry in its lower part (under 0 m a.m.s.l.);
- 92 • a concrete pile and a coarse concrete wall between 0 m and 9.50 m;
- 93 • a backside backfill forming the major part of the quay volume above 0
94 m.

95 Both quays are covered with pavement having an approximate thickness
96 of 10 cm (figures 1a and b). Various indices can be observed at the surface
97 of the structures :

- 98 • Pavement (the main constituent of the quay);
- 99 • Metallic materials (such as railways);
- 100 • Unconsolidated backfills employed to fill previous subsidences ;
- 101 • Dark asphalt patches ;
- 102 • Sparce local vegetation.

103 **3. Field survey and methodology**

104 *3.1. Photogrammetric survey*

105 Here, our first objective is to detect surface deformations associated to po-
106 tential subsurface voids, using altimetric data. To do so, a photogrammetric
107 survey of the EQ and WQ was performed on October 2014. We used a drone
108 equipped with a SONY NEX-5R digital camera (verticallly positionned) and
109 acquiring images (4912*3264 px). The focal length of the camera is 16 mm
110 (35 mm equivalent : 24 mm) and the sensor size is 23,4 x 15,6 mm. The
111 survey was realized along a pre-defined flight plan, with a longitudinal ac-
112 quisition at a height above ground of 20 m (figure 4). This lead to a surface
113 image footprint of 30*20 m and a resolution of about 5 mm. The UAV flew
114 at a speed of $\approx 1 \text{ m} \cdot \text{s}^{-1}$, with longitudinal and transversal overlaps of the
115 images of 80 %. Finally, a total of 194 and 165 images was acquired for the
116 EQ and the WQ, respectively.

117 The altimetric maps of the quays were calculated using the photogram-
118 metric approach. The 3D reconstruction of a scene is realized from pho-
119 tographs taken at arbitrary angles (Quinn (1948)). For this purpose, the
120 open-source Apero-MicMac code developped by the French National Geo-
121 graphical Institute (IGN) was used (Deseilligny & Cléry (2011)). The pro-
122 cessing of the data follows three steps :

- 123 • Detection of keypoints and matching between images using the SIFT
124 algorithm (Lowe (2004)) (Tapioca module) ;
- 125 • Calibration of the camera's internal parameters and determination of

126 the 3D positions and orientations of the viewpoints (Snavely et al.
127 (2008)). This step also allows the user to georeference manually the
128 model using Ground Control Points (GCPs). At this stage, a 3D un-
129 densified point cloud is produced (TAPAS module);

- 130 • Dense matching : densification of the point cloud calculated during the
131 TAPAS processing (Furukawa & Ponce (2010)) (MALT module).

132 The Tapioca processing leads to the detection of an average value of 10000
133 keypoints per image and for each quay. After this step, the model was georef-
134 erenced thanks to Ground Control Points (GCPs) within the Tapas module.
135 For this purpose, we used 29 and 31 GCPs (visible targets from the uav) on
136 the EQ and WQ, respectively (figure). These points were georeferenced us-
137 ing a D-RTK GNSS receptor and were homogeneously placed on the quays.
138 The quality of the measurements was quantified by comparing these data
139 with those obtained using the leveling network of Le Havre Harbour. The
140 comparison was realized on 19 and 15 points for the WQ and EQ, respec-
141 tively. As a result, for the WQ, the mean error is $0.008 \text{ m} \pm 0.007 \text{ m}$ in the
142 X direction, $0.018 \text{ m} \pm 0.012 \text{ m}$ in the Y direction and $0.043 \text{ m} \pm 0.018 \text{ m}$ in
143 the Z direction. For the EQ, the mean error is $0.007 \text{ m} \pm 0.007 \text{ cm}$ in the X
144 direction, $0.021 \text{ m} \pm 0.007 \text{ m}$ in the Y direction and $0.027 \text{ m} \pm 0.017 \text{ cm}$ in
145 the Z direction. Finally, during the Tapas processing, the residual error for
146 the 3D positioning and orientation of the Tapas module is 0.8 pixel for both
147 quays (this value has to be lower than 1 pixel).

148 *3.2. TIR survey*

149 The TIR method allows to map the surface temperatures of a surface
150 using a thermal camera. For a given soil, when no flow occurs, many ther-
151 mophysical and geometrical properties may control the diurnal cycle thermal
152 signal : the thermal inertia I ($J. m^{-2}.K^{-1}.s^{-1/2}$) is the principal parameter
153 controlling the amplitude and the shape of these thermal oscillations (Wat-
154 son (1975), Mellon et al. (2000), Putzig & Mellon (2007)) and albedo (or
155 reflectivity) controls the average temperature (figure 5). Eventually, when
156 steep topography is present (for instance, with crest and valleys), the surface
157 temperatures may also be influenced by the geometry of the surfaces, due
158 to their orientation regarding the incident solar radiation (Whiteman et al.
159 (1989), Khesin & Eppelbaum (1994), Eppelbaum et al. (2014)). In the case
160 of the WQ and EQ, the absence of steep slopes prevents from the generation
161 of important thermal gradients associated to topography.

162 Thermal inertia represents the ability of the material to conduct and store
163 the incident solar radiation at depth during the day, and re-emit this energy
164 during the night. It depends on the porosity and the pore size. For instance,
165 rocks or compacted soils typically have high values of thermal inertia, while
166 loosely packed soils with fine grains exhibit lower values of thermal inertia.
167 Thus, when observed with a thermal camera, compacted soils are warmer
168 than loosely packed materials during daytime, while the opposite situation
169 is observed during nighttime. This characteristic has been used for years
170 with success for geological mapping (SABINS (1969), Watson (1973), Watson
171 (1975), Majumdar (2003), Nasipuri et al. (2005)), using satellite and airborne

172 thermal imagery. Thermal inertia is defined as a combination of the thermal
173 conductivity k ($\text{W}\cdot\text{m}^{-1}\cdot\text{K}^{-1}$), the density ρ ($\text{W}\cdot\text{m}^{-3}$) and the heat capacity
174 c_p ($\text{W}\cdot\text{kg}^{-1}\cdot\text{K}^{-1}$) :

$$I = \sqrt{k\rho c_p} \quad (1)$$

175

176 As the volumetric heat capacity (ρc_p) has a low variability for soils and
177 rocks [Mermoud, 2006], the principal factor controlling the thermal inertia I
178 is thus the thermal conductivity k .

179 In the presence of a flow, the influence of surface properties (thermal iner-
180 tia and albedo) on the temperature is reduced, due to the mass movement of
181 the fluid bringing or extracting heat from the soil. The efficiency of the heat
182 transfer depends on the nature of the fluid and the soil (in fact their volumet-
183 ric heat capacity ratio and their thermal conductivity) and also on the Darcy
184 velocity of the fluid, controlled by the permeability of the soil (Antoine et al.
185 (2009)). Thus, we define a thermal anomaly as a thermal behavior which
186 cannot be explained by surface properties such as thermal inertia or albedo.
187 This methodology has already been successfully used in some of our works
188 for hydrogeological applications from field works and satellite data (Antoine
189 et al. (2009), Antoine et al. (2017), Lopez et al. (2016)).

190 A thermal infrared campaign was realized at the same moment than
191 the photogrammetric one (i.e. in October 28th 2014). An Optris PI400
192 Lightweight thermal camera was used on-board the UAV to measure the sur-

193 face temperature of the soil from 7h15 am to 16h30 pm (sunrise around 7h30
194 during the survey). This led to the acquisition a time series of 9 images for
195 each quay. During the survey, the weather was clear (thus allowing the flight
196 of the drone), with a small amount of rain and moderate precipitation was
197 observed from October 20th to 24th on the Harbour. During this month,
198 the atmospheric temperature varied from 10° to 17° and the monthly mean
199 temperature remained quasi-stable.

200 The PI400 thermal camera uses an uncooled microbolometer technology
201 to measure radiations in the range [7-14 μm] and its thermal sensitivity is
202 0.08°. The size of the sensor is 382*288 pixels sensor, with a Field of View
203 (FOV) value of 29° x 22°. Thus, at a height of 150 m, the camera is able to
204 acquire a thermal scene of a whole quay, with a pixel size of 40 cm .

205 The surface temperatures measured by the camera are corrected from the
206 effects of the relative humidity of the air, the atmospheric temperature and
207 the distance of the target using the relationships provided by Optris. Most
208 of the building materials have emissivity parameter ranging from 0.90 to 0.96
209 [Thermoworks, 2018]. Thus, a mean emissivity of 0.93 was used to correct
210 the surface temperature from the effect of emissivity. The thermal images
211 were then orthorectified using the ARCGIS software and georeferenced with
212 the soil targets, as well as remarquable objets on the thermal images (rails,
213 quai borders, etc...).

214 4. Altimetry of the quays

215 The figure 6 displays the altimetric maps obtained after the photogram-
216 metric processing, as well as longitudinal and tranverse profiles of the EQ
217 and WQ, respectively (P1 and P2, figures 6b and d). Each map is overlaid
218 with a simplified internal structural characteristics of the quay. Both quays
219 exhibit an increase of the altitude towards land, from 9.32 m to 9.90 m in
220 the case of the EQ and from 9.41 to 10 m for the WQ. The EQ longitudinal
221 profile shows the presence of four altimetric anomalies at the front of the
222 quay (e.g. depressions named AAE1 to AAE4). These depressions have a
223 nearly similar morphology with the same depth-over-horizontal distance ra-
224 tio. The largest subsidence reaches up to 15 cm (AAE3) over a distance of
225 30 m. The deepest one is AAE1, with a vertical amplitude of 10 cm over a
226 distance of 2 m in the transverse direction (i.e. a slope of (i.e. a slope of 3°)).
227 Interestingly, the subsidences occur at the boundary between the backfill and
228 the front concrete wall (figure 3). For the WQ, two topographic depressions
229 are observed at the back of the WQ (AAW1 and AAW2), with an amplitude
230 reaching 10 cm over a distance of ≈ 2 m (i.e. a slope of 3°). Here, the
231 subsidence occurs at the boundary between the quay and the land. Note
232 that the depressions are not symmetric, with the presence of a steep slope
233 (the Southern one) and a softer one (Northern slope). This morphology may
234 reflect the heterogeneous conditions within the quays (from a lithological,
235 structural and geomechanical point of view).

236 5. Observation of surface temperatures

237 In this section, temperature maps of the WQ and EQ are presented. As
238 mentionned in section 3.2, a time series of 9 images was acquired for each
239 quay. For the sake of clarity, we only show four snapshots acquired at 7h45,
240 10h40, 13h and 16h30 (figure 7) :

- 241 • The first temperature map presented here was obtained at 7h45. It
242 reveals temperatures with a minimum of 5.4°C and a maximum of
243 11.5°C for the quays (figures 7a and 7b). At that time, the most
244 distinguishable objects on the WQ and EQ are the railways (yellow
245 to red colored lineaments on the image), with a temperature around
246 7°C
- 247 • At 10h40, more than 2 hours after sunrise, the soil is warming up (fig-
248 ures 7c and 7d). The surface temperature is observed in the range
249 $[7.5^{\circ}\text{C}-14.5^{\circ}\text{C}]$. Asphalt patches appear in red on the WQ and EQ
250 (warmer objects), with temperatures between 10°C and 14°C : indeed
251 their very low albedo permits the absorption of an important amount
252 of solar radiation during the morning and their quick warming. Sur-
253 prisingly, elongated cold areas appear on both quays (TAW1, TAW2
254 and TAE1), with a direction parallel to the structure and with a tem-
255 perature around 9°C . It is of note that this signal is not distinguishable
256 in the early morning (7h45).
- 257 • During the afternoon (13h and 16h30 , figures 7e to 7h), this cold zone

258 become more and more noticeable on the WQ with a temperature of
259 about 14°C, i.e. with a maximum temperature contrast reaching 2-3°C,
260 compared with the surrounding environment. The same phenomenon is
261 observed on the EQ : three cold areas (TAE1 to TAE3) are perceptible
262 at the front of the structure at 13h, with some of them parallel to the
263 direction of the quay (TAE1 and TAE2). They reach a similar temper-
264 ature contrast than the WQ with their surrounding environment, i.e.
265 about 2-3°C. In the following sections, we assess the influence of ther-
266 mal inertia and albedo on the generation of the surface temperatures
267 of the WQ and EQ and intent to explain the origin of the TAE1-TAE3
268 and TAW1-TAW2 cold zones. It is of note that the size of these ther-
269 mal anomalies is at least 2 m in the transverse direction, i.e. easily
270 analysable given the resolution of our temperature images (0.4 m).

271 *5.1. Temperatures explained by surface properties*

272 Figure 8 displays the altimetry data (figures 8a and d), the thermal images
273 acquired at 13h (figures 8b and e) and a classification of all indices present
274 on the WQ and EQ (figure 8c and f). These images are superimposed with
275 a simplified structural map of the quays. As expected, at the first order, the
276 essential part of the thermal patterns observed in section 5 can be explained
277 by the presence of different materials on the quays (i.e. asphalt, backfill,
278 metal, concrete or vegetation) (figures 8c and f).

279 The figure 9 displays several exemples of temperatures controlled by sur-
280 face properties. The influence of thermal inertia may be seen in figure 9a (as

281 shown theoretically in figure 5a) : due to their high thermal inertia compared
282 to the pavement, the railways appears warmer before sunrise and cooler dur-
283 ing daytime (with a contrast up to 1.5°C). Such observation is consistent
284 with several previous results obtained using a TIR camera (Watson (1975),
285 Sabins (2007), Mellon et al. (2000), Antoine et al. (2009)). On the other hand,
286 dark colored material like asphalt having a low albedo ($A=0.07$) may appear
287 warmer than the pavement ($A=0.23$) during the whole measurement time
288 (figure 9b, as presented theoretically in figure 5b) (Watson (1975), Sabins
289 (2007)).

290 Finally, vegetation also have a distinct thermal behavior, as illustrated in
291 figure 9c. Plants appear slightly cooler than the pavement during daytime
292 (from noon), while being warmer during nighttime. In that case, as described
293 by Sabins (2007) and Whitehead et al. (1986), transpiration lowers the leaf
294 temperature and makes vegetation appearing cooler than soils during day-
295 time. During the night, the insulating effect of air within the leaves and the
296 important water content allow to retain heat, resulting in warm nighttime
297 signature. Finally, it is worth noting the conflicting effect of transpiration
298 with thermal inertia in the vegetation surface temperature. Indeed, plants
299 have a lower thermal inertia than soils due to 1) lower densities and ther-
300 mal conductivities of foliage compared to mineral constituents (Gates (1980)
301 and Hillel (1982)), and 2) lower heat capacities for foliage compared to both
302 mineral constituents and organic matter in soil (Hillel (1982)).

303 *5.2. Temperatures not explained by surface properties*

304 When closely analyzing the figures 8c and f, TAE1, TAE2, TAW1 and
305 TAW2 are all located on the same pavement. Thus, thermal inertia variations
306 can not be invoked to explain the important temperature constrasts of 2-3°C
307 on the same material. Figures 9d and 9e display an exemple of temperature
308 evolution for TAW1 and TAE1. These signals have a similar evolution, being
309 several degrees cooler than the pavement during nighttime and daytime, which
310 is not consistent with a variation controlled by thermal conductivity.

311 The thermal behavior of TAE3 is interesting (figure 9f) : first, it is char-
312 acterized by a cold anomaly like the others, but the material is different (i.e.
313 backfill, figures 8e and f). Second, TAE3 is cooler than the surrounding pave-
314 ment during daytime. Nevertheless, unconsolidated/loosely packed materials
315 are known to have a lower thermal inertia than solid rocks like pavements (due
316 to a lower thermal conductivity and density, (Mellon et al. (2000), Putzig &
317 Mellon (2007)). As a consequence, they may appear warmer than solid rocks
318 during the day, which is the opposite of our observation. This last finding
319 definitely rules out the role of thermal inertia on the signal variation.

320 The figure 10 presents a zoom on the surface at the locations of TAW1,
321 TAW2, TAE1 and TAE2. It is clear that no particular contrast in color
322 is observed on the pavement able to explain the thermal spatial variations.
323 Moreover, as the pavement is made with the same limestone material, it is
324 doubtful that emissivity variations may explain such thermal contrasts for
325 both quays.

326 Our data suggest a good correlation between the thermal anomalies and

327 the topographic depressions present on both quays, except for AAE3, where
328 no significant thermal contrast is observed within the backfill (even though
329 the material thermally evolves in the same way than TAE3). The figure 11
330 presents an example of comparison between a transverse topographic profile
331 and a thermal profile for the WQ (T1, figures 11a and b) and the EQ (T2,
332 figures 11c and d). Interestingly, the minimum of temperature appears to
333 be spatially related with the flank of the deformations for both cases. This
334 finding may not be justified by a thermal effet associated to the topography
335 of these depressions for several reasons : 1) because of the weak amplitude
336 of the subsidences, preventing for the occurrence of shadows (section 4) and
337 2) because of the E-W orientation of the quays, which may receive the same
338 amount of energy on their whole surfaces during daytime. This last idea is
339 difficult to reconcile with the presence of E-W elongated thermal anomalies
340 on the quays.

341 Finally, together, these observations are correlated with the structure of
342 the quays, as mentionned in section section 4 and illustrated in figures 3
343 and 11 : boundary between the internal concrete wall and the backfill for
344 the EQ and boundary between the quay and the land for the WQ, inducing
345 elongated thermal anomalies. Such limits may represent fragile areas for
346 the generation of subsurface voids. In the next sections, we investigate the
347 influence of subsurface process on the thermal signal.

348 **6. Thermal influence of an insulating subsurface cavity within the**
349 **quays : 2D conductive-radiative numerical modelling**

350 The previous section shows that the observed TAW1, TAW2, TAE1 and
351 TAE2 thermal anomalies 1) may not be explained neither by a contrast of
352 thermal inertia associated to a different material, nor by albedo contrasts
353 and 2) are correlated with topographic depressions associated to potential
354 subsurface cavities or decompressed areas. As a consequence, a subsurface
355 process must be associated to this anomalous signal. In order to show the
356 influence of a thermally insulating body within the quay, a 2D conductive-
357 radiative numerical simulation of the EQ is realized. Our objective is to
358 assess the first-order surface temperature signal induced by a simplified air-
359 filled area at depth.

360 *6.1. Equations and surface energy budget*

361 In the following, we review the basic 2-D equations describing the diurnal
362 temperature profile $T(x,z,t)$ through the quay (x designates the horizontal
363 distance (m), z represents the depth (m) and t the time (s), respectively). We
364 solve the transient conductive heat equation with the finite elements scheme
365 (second order in time and space) for a soil layer of thickness $d=9.5$ m, with
366 a spatial resolution of 1 cm and time step of 5 min. The astronomical, ge-
367 ographical and optical parameters of the model, their assumed values and
368 their units are summarized in Table 1. This model is based on the equations
369 published in Antoine et al. (2009), and extended in 2D in this study, using the
370 COMSOL Multiphysics numerical suite (Heat Transfer module). The simu-

371 lation were done for a transverse section of the quay to save computer time.
 372 This assumption may be valid from a physical point of view, as the length
 373 over width ratio of the quay is important. The simulations, performed for the
 374 EQ, take into account the geometry of the structure and a scheme of the nu-
 375 merical model is given in figure 12. The quay exhibits a complex geotechnical
 376 configuration (including backfill, limestone rubles, granite rubles, limestone
 377 pavement, coarse concrete wall) (figure 3). In order to simplify the modelling,
 378 four categories of dry materials were considered : limestone (C1, C2, C5 in
 379 figure 12), concrete (C3), granite (C4) and backfill (C6). The values of the
 380 physical parameters used for these materials (thermal conductivity, density,
 381 heat constant) are given in table 2.

382 The transient temperature in the soil, $T(x, z, t)$ is solution of the equation:

$$\frac{\partial T(x, z, t)}{\partial t} = \kappa \left(\frac{\partial^2 T(x, t)}{\partial x^2} + \frac{\partial^2 T(z, t)}{\partial z^2} \right) \quad (2)$$

383 where x is the horizontal distance (m), z is the depth (m), t is the time (s)
 384 and κ is the thermal diffusivity of the soil , which is related to the thermal
 385 conductivity k , the heat capacity C_p and the mass density ρ of the soil
 386 through:

$$\kappa = \frac{k}{\rho h_s} \quad (3)$$

387 A zero heat flux condition is set at the lower boundary of the model. For
 388 a flat surface, the surface temperature during a diurnal cycle depends on
 389 the solar heat flux (I_s), the soil radiative emission (I_e), and the atmospheric

390 radiative flux (I_l). Thus, the boundary condition at the surface is given from
 391 the balance of solar, atmospheric and emitted radiations (Watson (1973)):

$$k \frac{\partial T(z=0, t)}{\partial t} = I_s - I_e + I_l \quad (4)$$

392 The solar flux I_s absorbed by the surface verifies:

$$I_s = (1 - A) S_0 C \cos(Z) \quad (5)$$

393 where A is the surface albedo and S_0 is the solar constant. C is fraction of
 394 the incident power arriving at the soil including the direct sun light and the
 395 diffuse radiations for a cloudy sky. Z is the zenith angle of the sun which can
 396 be estimated from the latitude ϕ of the observation point (Watson (1973)):

$$\cos(Z) = \cos \phi \cos \delta \cos(\theta) + \sin \phi \sin \delta \quad (6)$$

397 where δ is the solar declination as a function of the number of day in
 398 Jovian year J (Duffie & Beckman (1980)) and is expressed here in radians:

$$\delta = 0.409 \sin\left(\frac{2\pi}{365} J - 1.39\right) \quad (7)$$

399 The longitude angle θ expressed also in radians corresponds to the time
 400 t in hours past noon:

$$\theta = 2\pi * \frac{t}{24} \quad (8)$$

401 Then, the thermally emitted flux from the surface I_e is given by:

$$I_e = \epsilon\sigma T^4 \quad (9)$$

402 where ϵ is the soil emissivity averaged in the thermal infrared wavelengths
 403 and $\sigma = 5.67 \times 10^{-8} \text{ JK}^{-4}\text{m}^{-2}\text{s}^{-1}$ is the Stefan-Boltzman constant. The
 404 thermal radiations from the atmosphere I_l are approximated following the
 405 empirical relation (Brunt (1932)):

$$I_l = \sigma T_a^4 (0.55 + 0.65 * \sqrt{e_a}) \quad (10)$$

406 where T_a is the air temperature in Celsius degrees and e_a is the saturation
 407 pressure of water in the air expressed in bar. $T_a(t)$ is approximated by
 408 *Jansson* [1998]:

$$T_a(t) = T_0 + \frac{1}{2}T_{amp} \cos \frac{2\pi(t - t_{ph})}{P_{dc}} \quad (11)$$

409 where T_0 is the mean air temperature during the diurnal cycle, and T_{amp}
 410 is the contrast of temperature between day and night as measured during
 411 the experiment. P_{dc} represents the duration of the diurnal cycle and t_{ph}
 412 the time shift between the maximum of the solar incident radiations and the
 413 maximum air temperature. This model results in a minimum air temperature
 414 at the sunrise and a maximum air temperature at t_{ph} after the zenith. Finally,
 415 e_a verifies the empirical law [Deffie and Beckman, 1980]:

$$e_a = 0.6108 \exp\left(\frac{17.27 * T_a(t)}{T_a(t) + 237.3}\right) \quad (12)$$

416 The lower boundary of the modelling box is considered to be the Mean
 417 Lower Low Water level (MLLW) (see figure 3), where the ocean level is the

Solar constant	S_0	1367 W m^{-2}
Direct + diffuse energy fraction at the soil	C	0.5
Latitude of Le Havre Harbour	λ	$20^\circ S$
Day number of the year (October, 28th)	J	113
Solar declination	δ	0.2 rad
Emissivity	ε	0.93
Stefan-Boltzman Constant	σ	$5.67 \times 10^{-8} \text{ W m}^{-2} K^{-4}$
Air thermal conductivity	k_a	$2 \times 10^{-2} \text{ W m}^{-1} K^{-1}$
Mean air temperature	T_0	$12^\circ C$
Amplitude of the air temperature	T_{amp}	$7.5^\circ C$
Phase shift	t_{ph}	3600 s
Duration of the diurnal cycle	P_{dc}	86400 s

Table 1: Physical parameters and units related to the conductive-radiative model.

Density of the limestone (C1, C2 and C5)	ρ_b	2500 $kg\ m^{-3}$
Limestone heat constant	c_b	830 $J\ kg^{-1}\ K^{-1}$
Limestone thermal conductivity	k_b	1.26 – 1.33 (1.3) $W\ m^{-1}\ K^{-1}$
Density of the concrete (C3)	ρ_b	2300 $kg\ m^{-3}$
Concrete heat constant	c_b	1100 $J\ kg^{-1}\ K^{-1}$
Concrete thermal conductivity	k_b	1 – 1.8 (1.5) $W\ m^{-1}\ K^{-1}$
Density of the granite (C4)	ρ_b	2600 $kg\ m^{-3}$
Granite heat constant	c_b	770 $J\ kg^{-1}\ K^{-1}$
Granite thermal conductivity	k_b	1.7 – 4 (3) $W\ m^{-1}\ K^{-1}$
Density of the backfill (C6)	ρ_b	1500 $kg\ m^{-3}$
Backfill heat constant	c_b	1000 $J\ kg^{-1}\ K^{-1}$
Backfill thermal conductivity	k_b	0.8 – 2.4 (1.5) $W\ m^{-1}\ K^{-1}$

Table 2: Physical parameters and units related to the materials used in the numerical model (from EngineeringToolbox (2003)) and Javadi et al. (2018)). Concerning the thermal conductivities, the values in bracket are the ones taken for the modelling.

418 lowest. Thus, in this case, the presence of unsaturated areas within the quay
419 are the most probable (with high thermal conductivity contrasts between
420 the soil and air). At this level, the temperature of the lower boundary of
421 the structure is considered as constant ($10^{\circ}C$) at a first approximation. To
422 simulate the presence of a cavity within the medium, we introduce a simplified
423 vertical air-filled zone at the back of the concrete material (figures 3). The
424 implementation of this zone at such location may be understandable from a
425 geotechnical point of view, since the backfill is the most probable material
426 subject to cavities, voids or decompressed areas, due to the withdrawal of fine
427 grained materials, when water enters the structure. It is also consistent with
428 the thermal observations, as the TAE1 and TAE2 anomalies are found at the
429 boundary between the concrete and the backfill and are elongated along this
430 boundary (figures 3 and 7b). Finally, this air-filled case represents a good
431 candidate for the simulation of important spatial variations of temperature
432 within the medium, because the important contrast of thermal conductivity
433 between air and rock.

434 *6.2. Numerical results*

435 In this section, we present several simulations for the EQ and for 3 differ-
436 ents cases as the depth of the potential voids is not known : 1) absence of
437 cavity within the quay; 2) presence of a cavity at 3 m-depth ; 3) presence of
438 a cavity at 1 m-depth. For each case, we present the 2D thermal field within
439 the EQ (figures 13 a, c and e), as well as a temperature profile at the surface
440 (figures 13 b, d and f) calculated at 13h (for more thermal contrasts). The

441 figure 13a presents the 2D temperature behavior of the EQ in the absence
442 of cavity. As the result is presented at 13h, the surface is the hottest part
443 of the medium. The heat diffuses within the quay from the surface up to
444 a depth of ≈ 2 m. The isotherms are very slightly deformed at the front
445 of the quay, due to the thermal conductivity contrast between the concrete
446 (present at the front of the quay) and the backfill (figure 3). As the thermal
447 conductivity is higher in the concrete material at depth, a slight decrease of
448 the surface temperature is generated in this part of the quay (figures 16a and
449 b). Such temperature difference between the concrete and the backfill (here,
450 less than 0.5°C) is obviously impossible to subtract from the diurnal cycle.
451 Finally, the heterogeneous temperature field within the quay is illustrated
452 by the vertical profile given in figure 14a, where temperature variation up to
453 15°C can be encountered, due to the thermal conductivity contrasts within
454 the structure.

455 The second case represents the thermal behavior of the quay when a cav-
456 ity is present at 3-m depth. As said in the previous section, it consists of
457 a vertical zone having the thermal conductivity of the air, located within
458 the backfill just at the back of the concrete. The general thermal pattern is
459 similar to the first case, but the isotherms are deformed within and above
460 the cavity, as it acts as a thermal insulator within the medium (figures 13c).
461 At the surface, the temperature decreases from the back to the front of the
462 quay, with a maximum temperature contrast of 0.5°C (figures 13d), but the
463 temperature variation above the cavity is not significant. Nevertheless, it is
464 interesting to note that in comparison with the model without cavity, the

465 surface horizontal thermal gradient is more important in this case (increase
466 of temperature with a shorter wavelength). This spatial variation may be due
467 to the deformation of the isotherms associated with the insulating body at
468 depth. However, such increase in temperature and variation in the shape of
469 the temperature profile are likely difficult to observe with a thermal camera,
470 considering the amplitude of the diurnal cycle. The vertical temperature pro-
471 file shown in figure 14b is slightly shifted towards higher temperatures above
472 the cavity. Although the general shape of the signal remains controlled by
473 the thermal conductivities of the structure within the quay, the temperature
474 profile is clearly modified when penetrating within the air-filled area. Such
475 change is due to the high contrast between the air and the materials of the
476 EQ.

477 The last case displays the thermal behavior of the structure with a cavity
478 located at 1-m depth (figures 13e and f), i.e. very close to the surface.
479 Here, the subsurface isotherms are strongly deformed, due to the presence of
480 the cavity (figures 13e). At the surface, the temperature profile follows the
481 general thermal trend of the previous case (lowest temperatures at the front
482 of the quay with a similar short wavelength), but the maximum of temperature
483 is found just above the cavity. The maximum temperature contrast is 0.9 °C
484 with the front of the quay and less than 0.4 °C with the back of the structure
485 . This result is consistent with the observations of V. Eppelbaum (2007), who
486 found a warm zone (temperature anomaly of 0.3°C) just above a 1 m-depth
487 underground cavity, using 40 cm-depth temperature sensors (figure 15). Our
488 modelling tends to show that a cavity close to subsurface may produce a

489 thermal signal by its own, due to the 2 order-magnitude difference between
490 the thermal conductivities of the air and of the soil. Indeed, the lowest is
491 the depth, the highest is the amplitude of the thermal anomaly. It is of note
492 that the thermal effect of such insulating zone for this given structure remains
493 limited (less than 1 °C) up to a depth of 1 m and probably not enough to
494 be currently detected. In that case, the vertical temperature profile given in
495 figure 14c is drastically modified by the air-filled area. Interestingly, in the
496 first meter below the surface, the shape of the signal is very different from the
497 3 m-depth case, as the thermal perturbation induced by the cavity interacts
498 with the daily surface heat waves propagating through the pavement and
499 the backfill. Then, below one meter, the air-filled area generate a thermal
500 anomaly but with a whole shape still controlled by the thermal behavior of
501 the EQ.

502 These three simulations show that an air-filled cavity may directly in-
503 fluence the temperature pattern at the surface of the soil. At depth, the
504 isotherms are deformed at the vicinities of the air-filled cavity, due to the
505 high contrast of thermal conductivities between air and rock. This situation
506 may induce a variation of the surface temperature pattern in two ways 1) an
507 increase of the thermal gradient (here by one order of magnitude : 0.02°C
508 m^{-1} without cavity to $0.2^{\circ}\text{C m}^{-1}$ for a location at 3 m depth) and 2) the
509 generation of a maximum of temperature reaching 0.4 to 0.9 °C above the
510 cavity at 1 m depth at mid-day. Despite the high thermal sensitivity of the
511 current thermal cameras ($\approx 0.01^{\circ}\text{C m}^{-1}$), such a signal clearly remains a
512 challenge to discriminate from the variations associated to the diurnal cycle.

513 In addition, our models were performed using the highest contrast between
514 thermal conductivities (air and rock), inducing the maximum temperature
515 contrast at the surface. In the case of high tides potentially generating water-
516 filled voids (with temperature contrasts between the rock and the liquid), the
517 situation may be more complex as 1) the thermal signal may be accordingly
518 attenuated, because of the reduced drop of thermal conductivity for water
519 ($0.02 \text{ W m}^{-1} \text{ K}^{-1}$ for air and $0.6 \text{ W m}^{-1} \text{ K}^{-1}$ for water) and 2) the absence
520 of thermal equilibrium between the water and rock may generate additional
521 thermal gradients. Following Turcotte & Schubert (2002), a time l^2/κ is re-
522 quired for temperature changes to propagate a distance l and for a thermal
523 diffusivity κ . Thus, taking a value κ in the range [$10^{-7} \text{ m}^2 \text{ s}^{-1}$ - $10^{-6} \text{ m}^2 \text{ s}^{-1}$]
524 for an unconsolidated material like backfill, and a value l of 3 m, the time
525 needed for the temperature changes arriving at the surface is in the range
526 [3 months - 3 years]. For a value l of 1 m, this time is reduced in the range
527 [10 days - 3 months]. Such values show that a thermal signal associated to
528 water within the water may be mostly masked by seasonal temperature vari-
529 ations. Finally, the results show that the generation of a warm area above
530 the cavity is inconsistent with our observations on the WQ and the EQ. In
531 the next section, an alternative physical phenomenon is suggested to explain
532 the the cold areas associated to the deformations of the quays.

533 **7. On the thermal influence of potential fluid flows within the WQ**
534 **and EQ**

535 In the previous sections, we have shown that most of the thermal signal
536 of the EQ and WQ may be explained by surface indices (surface properties).
537 However, cool areas persist during daytime that can not be explained 1) by
538 contrasts associated to thermal inertia, albedo or topography and 2) nor by
539 the direct thermal effect of a subsurface cavity located at shallow depth.
540 However, surprisingly, these observations are correlated with deformations,
541 as well as the structure of the quays.

542 Other processes associated to the presence of a fluid have been searched
543 to explain these temperature drops. For instance, water standing at the sur-
544 face is cooler during the day and warmer during the night (Sabins (2007)).
545 Nevertheless, the presence of a slope at the location of the thermal anomaly
546 prevents for any stay of water, ruling out this hypothesis. Possible drainage
547 of the fluids within the quays implies the generation of a preferential vertical
548 permeability field. In the case of the WQ and EQ, thermal anomalies are lo-
549 cated on the flanks of local subsidences (figure 11). From a mechanical point
550 of view, it is known that the slopes of such depressions are subject to exten-
551 sive stresses, while the center (topographic low) may be rather under com-
552 pressive forces (figure 16) (Berenger et al. (2014), Al-Halbouni et al. (2018),
553 Al-Halbouni et al. (2019), Yin et al. (2019)). Consequently, these extensive
554 stresses tend to generate a preferential vertical permeability within the joints
555 of the pavement (through micro-fracturation), while the compressive forces

556 may close the fractures at the center of the topographic depressions. These
557 micro-fractures may not appear everywhere around the deformation, as the
558 medium constituting the quays is highly heterogeneous, with the presence
559 of backfill and concrete.

560 We propose an alternative cooling mechanism induced by water infiltration
561 through micro-fractures (in the pavement for TAE1, TAE2, TAW1 and TAW2
562 and within the backfill for TAE3) to explain our observations. Indeed, the
563 analysis of meteorological data at stations close to Le Havre Harbour (Cap
564 de la Heve and Octeville) indicates that the October month was particularly
565 rainy, with intermittent to continuous rainfall (figure 17). Important rainfall
566 occurred until October 16h (up to 24 mm), while moderate precipitation was
567 recorded from October 20th to October 24th for Le Havre city (from 1.6 to
568 4 mm/h). During the following days, the weather was strongly disturbed
569 with a high humidity content on the atmosphere (around 80 % of relative
570 humidity) and an important decrease of the hourly solar radiation (from
571 15h of sunshine on October 22th to 7h on October 28th) and small rain on
572 October 28th .

573 Many works report changes in soil temperature caused by percolating
574 water, following rainfall or irrigation (Callendar (1895), Franklin (1921),
575 Shul'gin et al. (1958)). Wierenga et al. (1979) experimentally and numeri-
576 cally characterized the thermal effect of infiltration on the shallow subsurface.
577 He measured the temperatures of a soil irrigated with cool (4°C) and warm
578 (21°C) water, at different depths (surface to 20 cm). The author shown that
579 irrigation, whatever the temperature of the water, results in lowering the

580 soil temperature below those of non irrigated soil during several days due to
581 Darcy flow, as displayed in figure 18. Eventually, the thermal anomaly can
582 persist a longer time below 20 cm depth, due to thermal diffusion. Wierenga
583 et al. (1979) explained this observation by heat tranfer between occuring by
584 water movement. The cooling of the soil during water infiltration is also de-
585 scribed in the numerical results of Lopez et al. (2016), for water flow within
586 a sedimentary basin.

587 In the case of Le Havre harbour, we propose that the autumn rain in
588 Normandy penetrates the soil of the quays through micro-fractures located
589 on the flancks of the deformations. This infiltration may induce a cooling of
590 the medium by several degrees Celcius (Wierenga et al. (1979)), due to the
591 highest Darcy velocity of the water within the fissures, compared to the rest
592 of the quay. During infiltration, the Darcy velocity is controlled by the effec-
593 tive permeability K of the medium (m^2), defined as $K=d^3/12f$ where d is the
594 fissure aperture (m) and f is the spacing between fissures (m). For an aper-
595 ture of 0.1 mm and a spacing $f=1$ m, $K= 10^{-13} m^2$, while this value drops to
596 $10^{-10} m^2$ when $d=1$ mm, i.e. a range comparable to the permeability of the
597 sand. Heat transfer between rock and water is enhanced due to the down-
598 ward movement of the fluid and its important volumetric thermal capacity
599 $\rho_w c p_w$. As illustrated in figure 18, this cooling may last several hours after
600 the occurence of infiltration before equilibrium. Eventually, during/after the
601 infiltration process, the evaporation of the water remained stuck on the walls
602 of the fissures by surface tension may also participate to the persistence of
603 the cooling of the medium (Geiger (1965), Van Bavel & Hillel (1976)), de-

604 pending on the incoming solar radiation, the atmospheric water content and
605 temperature, the presence of wind and the amount of water available within
606 the soil.

607 It is currently difficult for us to discriminate the relative influence of infil-
608 tration and evaporation on the surface temperatures. Besides, the following
609 elements may be highlighted. The detection of cold anomalies located on
610 the deformations was confirmed for both quays by a second campaign real-
611 ized in March 2015 19, just after rainy days. This is remarkable, considering
612 that the survey was performed during another season (and thus different ra-
613 diative, meteorological and soil temperature conditions). The 2015 survey
614 emphasizes several points : 1) the detection of thermal anomalies is repeat-
615 able using our methodology, 2) their morphology is comparable to 2014 and
616 3) important thermal contrasts are observed, similar to 2014, i.e. $\approx 3^{\circ}\text{C}$. In
617 that case, it is proposed that evaporation may influence the surface temper-
618 atures to a lesser extent than infiltration, considering the observed difference
619 in the daily average solar radiation in October (138 W/m^2) and March (219
620 W/m^2) in Le Havre city (see the irradiation Geographical Information Sys-
621 tem for Europe for details :). As the evaporation rate directly depends on
622 the incoming solar radiation, a different evaporation rate may be induced at
623 the surface and thus different temperature contrasts, which is not what we
624 observe.

625 Obviously, further investigations may lead with no doubt to a better
626 evaluation of the role of these two components (infiltration and evaporation)
627 on the thermal field. Numerical modelling may be improved in several ways

628 : 1) implementation of fluid flow in unsaturated media physics, taking into
629 account radiative surface boundary condition, 2) integration of meteorologic,
630 radiative and optical (albedo) field data as input for the modelling. For
631 instance, albedo maps may be obtained using pyranometers on-board drones
632 (Levy et al. (2018)) and considerably improve the description of the radiative
633 surface boundary condition and 3) implementation of radiative processes
634 for sloped surfaces to characterize the link between topography and surface
635 temperatures. Finally, analogical experiments may be realized on several
636 soils types in a climatic chamber in order to characterize the link between
637 infiltration, evaporation and thermal infrared observations. In this frame,
638 the combination of remote sensing and geophysical data (measuring electric
639 or dielectric parameters) may be useful to quantify the relationships between
640 water flow, evaporation rates and soil temperatures.

641 **8. Conclusions**

642 Visible and thermal infrared observations obtained with a light UAV are
643 presented on two port quays. Photographies are used to calculate altimet-
644 ric maps of the structures by means of the photogrammetric method, while
645 thermal images serve to monitor semi-diurnal temperature variations of the
646 surface. The analysis of the altimetric data reveals several deformations at
647 the surface of the WQ and the EQ and associated to potential subsurface
648 cavities/decompressed areas at depth. The study of thermal maps show that
649 the major part of surface temperatures observed on the WQ and the EQ
650 may be explained by thermal inertia and albedo. Nevertheless, five cold

651 areas (TAW1, TAW2 and TAE1 to TAE3) are revealed on the quays, not
652 explained by these parameters. These anomalies appear in the morning and
653 persist during the all day, with a temperature contrast with the surround-
654 ing environment ranging from 2 to 4°C. Alongside this observation, a clear
655 correlation is found between thermal anomalies, deformations identified on
656 the altimetric data and the structure of the quays. More precisely, the min-
657 imum of temperature of the cold regions are located on the flanks of the
658 deformations.

659 The origin of this correlation is then investigated. A simplified 2D model
660 is developed to quantify the direct surface thermal influence of a subsurface
661 cavity, when present at two different depths (3 m and 1 m below the surface).
662 These simulations show that 1) the gradient of the surface temperature may
663 vary when a subsurface cavity/decompressed area is present at depth ; 2)
664 a hot thermal anomaly is induced at the surface by a cavity/decompressed
665 area at depth during the day, which is inconsistent with our observations
666 and 3) the amplitude of the anomaly (less than 1 °C) may be too low to be
667 detected by TIR cameras, given the amplitude of the diurnal cycle. In this
668 study, we only made 2D simulations to assess the first order characteristics of
669 the thermal pattern, but 3D thermal patterns may clearly be present within
670 the medium, due to the complexity of the structures of the quays. Such con-
671 sideration must be taken into account in future works. We explain the cold
672 anomalies and their correlation with the deformations by the cooling induced
673 by infiltration and subsequent evaporation of water through micro-fractures,
674 permitting the persistence of the anomaly several hours after rainfalls. As

675 a consequence, we argue that the high permeability of the medium induced
676 by stresses within the medium when a cavity/decompressed soil is present
677 may control the surface temperatures observed on both WQ and EQ. To our
678 knowledge, this study is the first establishing a link between thermal anoma-
679 lies and surface deformations associated to subsurface cavities/decompressed
680 areas. Such result is made possible given the new capabilities of U.A.Vs,
681 able to monitor port quays and more broadly civil engineering structures at
682 high resolution, low cost and in a very flexible way. Finally, these methods
683 may also be very useful for the detection of subsurface voids in clayey soils,
684 where classical geophysical tools (like Ground Penetrating Radar) remain
685 inefficient.

686 **Acknowledgement**

687 This research project benefited from the support of the Grand Port
688 Maritime du Havre and from the French Ministry for the Ecological and
689 Inclusive Transition. We wish to thank both anonymous reviewers for their
690 very useful and constructive comments.

691 **References**

692 Al-Halbouni, D., Holohan, E., Taheri, A. et al. (2018). Geomechanical mod-
693 elling of sinkhole development using distinct elements: model verification
694 for a single void space and application to the dead sea area. *Solid Earth*,
695 *9*, 1341–1373.

- 696 Al-Halbouni, D., Holohan, E. P., Taheri, A., Watson, R. A., Polom, U.,
697 Schöpfer, M. P., Emam, S., & Dahm, T. (2019). Distinct element geome-
698 chanical modelling of the formation of sinkhole clusters within large-scale
699 karstic depressions. *Solid Earth*, *10*, 1219–1241.
- 700 Antoine, R., Baratoux, D., Rabinowicz, M., Fontaine, F., Bachlery,
701 P., Staudacher, T., Saracco, G., & Finizola, A. (2009). Ther-
702 mal infrared image analysis of a quiescent cone on piton de la
703 fournaise volcano: Evidence of convective air flow within an un-
704 consolidated soil. *Journal of Volcanology and Geothermal Re-*
705 *search*, *183*, 228 – 244. URL: [http://www.sciencedirect.com/](http://www.sciencedirect.com/science/article/pii/S0377027308006525)
706 [science/article/pii/S0377027308006525](http://www.sciencedirect.com/science/article/pii/S0377027308006525). doi:[https://doi.org/10.](https://doi.org/10.1016/j.jvolgeores.2008.12.003)
707 [1016/j.jvolgeores.2008.12.003](https://doi.org/10.1016/j.jvolgeores.2008.12.003).
- 708 Antoine, R., Finizola, A., Lopez, T., Baratoux, D., Rabinowicz, M., Delcher,
709 E., Fontaine, F. R., Fontaine, F. J., Saracco, G., Bachèlery, P. et al. (2017).
710 Electric potential anomaly induced by humid air convection within piton
711 de la fournaise volcano, la réunion island. *Geothermics*, *65*, 81–98.
- 712 Artugyan, L., Ardelean, A. C., & Urdea, P. (2020). Gpr and ert investigations
713 of karst structures at the buhui-cuptoare cave system, anina karst region
714 (banat mountains, romania). In A. Biswas, & S. P. Sharma (Eds.), *Ad-*
715 *vances in Modeling and Interpretation in Near Surface Geophysics* (pp. 19–
716 38). Cham: Springer International Publishing. URL: [https://doi.org/](https://doi.org/10.1007/978-3-030-28909-6_2)
717 [10.1007/978-3-030-28909-6_2](https://doi.org/10.1007/978-3-030-28909-6_2). doi:[10.1007/978-3-030-28909-6_2](https://doi.org/10.1007/978-3-030-28909-6_2).

- 718 Benavente, J., Vadillo, I., Liñán, C., Martínez-Moreno, F. J., Galindo-
719 Zaldívar, J., & Carrasco, F. (2017). Identification of vadose karst voids
720 and ventilation patterns coupling hydrochemical and geophysical methods
721 (maro spring, near nerja, southern spain). In P. Renard, & C. Bertrand
722 (Eds.), *EuroKarst 2016, Neuchâtel* (pp. 327–334). Cham: Springer Inter-
723 national Publishing.
- 724 Berenger, N., Flahaut, R., Mathon, D., Kreziak, C., & Marty, F. (2014).
725 Le diagnostic de stabilité des carrières souterraines abandonnées. guide
726 méthodologique.
- 727 Brunt, D. (1932). Notes on radiation in the atmosphere. i. *Quar-*
728 *terly Journal of the Royal Meteorological Society*, 58, 389–
729 420. URL: [https://rmets.onlinelibrary.wiley.com/doi/](https://rmets.onlinelibrary.wiley.com/doi/abs/10.1002/qj.49705824704)
730 [abs/10.1002/qj.49705824704](https://rmets.onlinelibrary.wiley.com/doi/abs/10.1002/qj.49705824704). doi:10.1002/qj.49705824704.
731 arXiv:<https://rmets.onlinelibrary.wiley.com/doi/pdf/10.1002/qj.49705824704>.
- 732 Callendar, H. (1895). Preliminary results of observations of soil temper-
733 atures with electrical resistance thermometers made at the mcdonald
734 physics building, mcgill university, montreal. *Transactions, Royal Soci-*
735 *ety of Canada, Second Series*, 1, 63–84.
- 736 Campbell, C. W., El Latif, A., & Foster, J. W. (1996). Application of ther-
737 mography to karst hydrology. *Journal of Cave and Karst Studies*, 58,
738 163–167.
- 739 Cardarelli, E., Cercato, M., Cerreto, A., & Di Filippo, G. (2009).

- 740 Electrical resistivity and seismic refraction tomography to de-
741 tect buried cavities. *Geophysical Prospecting*, 58, 685–695.
742 URL: [https://onlinelibrary.wiley.com/doi/abs/10.1111/j.](https://onlinelibrary.wiley.com/doi/abs/10.1111/j.1365-2478.2009.00854.x)
743 [1365-2478.2009.00854.x](https://onlinelibrary.wiley.com/doi/abs/10.1111/j.1365-2478.2009.00854.x). doi:10.1111/j.1365-2478.2009.00854.x.
744 arXiv:<https://onlinelibrary.wiley.com/doi/pdf/10.1111/j.1365-2478.2009.00854.x>.
- 745 Chang, L., & Hanssen, R. F. (2014). Detection of cavity migration and
746 sinkhole risk using radar interferometric time series. *Remote Sens-*
747 *ing of Environment*, 147, 56 – 64. URL: [http://www.sciencedirect.](http://www.sciencedirect.com/science/article/pii/S0034425714000674)
748 [com/science/article/pii/S0034425714000674](http://www.sciencedirect.com/science/article/pii/S0034425714000674). doi:[https://doi.org/](https://doi.org/10.1016/j.rse.2014.03.002)
749 [10.1016/j.rse.2014.03.002](https://doi.org/10.1016/j.rse.2014.03.002).
- 750 De Giorgi, L., & Leucci, G. (2014). Detection of hazardous cavities below
751 a road using combined geophysical methods. *Survey in Geophysics*, 35,
752 1003–1021.
- 753 Deseilligny, M. P., & Cléry, I. (2011). Apero, an open source bundle adjus-
754 tment software for automatic calibration and orientation of set of images.
755 In *Proceedings of the ISPRS Symposium, 3DARCH11*. volume 269277.
- 756 Duffie, J. A., & Beckman, W. A. (1980). Solar radiation. *Solar Engineering*
757 *of Thermal Processes*, (pp. 3–17).
- 758 Edmonds, C., Kennie, T., & Rosenbaum, M. (1987). The application of
759 airborne remote sensing to the detection of solution features in limestone.
760 *Geological Society, London, Engineering Geology Special Publications*, 4,
761 125–131.

- 762 EngineeringToolbox (2003). Thermal conductivity of selected materials and
763 gases. [available online]. URL: [https://www.engineeringtoolbox.com/
764 thermal-conductivity-d_429.html](https://www.engineeringtoolbox.com/thermal-conductivity-d_429.html).
- 765 Eppelbaum, L., Kutasov, I., & Pilchin, A. (2014). *Applied geothermics*.
766 Springer Berlin Heidelberg.
- 767 Franklin, T. B. (1921). Viii. the effect of weather changes on soil tempera-
768 tures. *Proceedings of the Royal Society of Edinburgh*, *40*, 56–79.
- 769 Furukawa, Y., & Ponce, J. (2010). Accurate, dense, and robust multiview
770 stereopsis. *IEEE Transactions on Pattern Analysis and Machine Intelli-
771 gence*, *32*, 1362–1376. doi:10.1109/TPAMI.2009.161.
- 772 Gates, D. M. (1980). Evaporation and transpiration. In *Biophysical Ecology*
773 (pp. 307–344). Springer.
- 774 Gaudin, D., Beauducel, F., Allemand, P., Delacourt, C., & Finizola, A.
775 (2013). Heat flux measurement from thermal infrared imagery in low-
776 flux fumarolic zones: Example of the ty fault (la soufrière de guadeloupe).
777 *Journal of Volcanology and Geothermal Research*, *267*, 47–56.
- 778 Geiger, R. (1965). The climate near the ground. *Cambridge: Harvard Uni-
779 versity Press, 1965, Rev. ed., .*
- 780 Gunn, D. A., Marsh, S. H., Gibson, A., Ager, G. J., McManus, K. B., Caunt,
781 S., & Culshaw, M. G. (2008). Remote thermal ir surveying to detect aban-

782 doned mineshafts in former mining areas. *Quarterly Journal of Engineering*
783 *Geology and Hydrogeology*, 41, 357–370.

784 Hillel, D. (1982). *Introduction to soil physics* New York, Academic Press.
785 Technical Report.

786 Javadi, H., Mousavi Ajarostaghi, S. S., Rosen, M. A., & Pourfallah, M.
787 (2018). A comprehensive review of backfill materials and their effects on
788 ground heat exchanger performance. *Sustainability*, 10. URL: [https://](https://www.mdpi.com/2071-1050/10/12/4486)
789 www.mdpi.com/2071-1050/10/12/4486. doi:10.3390/su10124486.

790 Jeffery, Z. E., Penn, S., Giles, D. P., & Hastewell, L. (2020). Iden-
791 tification, investigation and classification of surface depressions and
792 chalk dissolution features using integrated lidar and geophysical
793 methods. *Quarterly Journal of Engineering Geology and Hydro-*
794 *geology*, . URL: [https://qjegh.lyellcollection.org/content/](https://qjegh.lyellcollection.org/content/early/2020/02/20/qjegh2019-098)
795 [early/2020/02/20/qjegh2019-098](https://qjegh.lyellcollection.org/content/early/2020/02/20/qjegh2019-098). doi:10.1144/qjegh2019-098.
796 arXiv:<https://qjegh.lyellcollection.org/content/early/2020/02/20/qjegh2019-098>.f

797 Kaufmann, G., & Romanov, D. (2016). Structure and evolution of col-
798 lapse sinkholes: Combined interpretation from physico-chemical mod-
799 elling and geophysical field work. *Journal of Hydrology*, 540, 688
800 – 698. URL: [http://www.sciencedirect.com/science/article/pii/](http://www.sciencedirect.com/science/article/pii/S0022169416304127)
801 [S0022169416304127](http://www.sciencedirect.com/science/article/pii/S0022169416304127). doi:[https://doi.org/10.1016/j.jhydrol.2016.](https://doi.org/10.1016/j.jhydrol.2016.06.050)
802 [06.050](https://doi.org/10.1016/j.jhydrol.2016.06.050).

803 Kaufmann, G., Romanov, D., & Nielbock, R. (2011). Cave de-

804 tection using multiple geophysical methods: Unicorn cave, harz
805 mountains, germany. *GEOPHYSICS*, 76, B71–B77. URL:
806 <https://doi.org/10.1190/1.3560245>. doi:10.1190/1.3560245.
807 arXiv:<https://doi.org/10.1190/1.3560245>.

808 Khesin, B. E., & Eppelbaum, L. V. (1994). Nearsurface thermal prospecting:
809 Review of processing and interpretation. *GEOPHYSICS*, 59, 744–752.
810 URL: <https://doi.org/10.1190/1.1443632>. doi:10.1190/1.1443632.
811 arXiv:<https://doi.org/10.1190/1.1443632>.

812 Kim, J.-W., Lu, Z., & Kaufmann, J. (2019). Evolution of sinkholes over wink,
813 texas, observed by high-resolution optical and sar imagery. *Remote Sens-*
814 *ing of Environment*, 222, 119 – 132. URL: <http://www.sciencedirect.com/science/article/pii/S003442571830587X>. doi:[https://doi.org/](https://doi.org/10.1016/j.rse.2018.12.028)
815 [10.1016/j.rse.2018.12.028](https://doi.org/10.1016/j.rse.2018.12.028).
816

817 Kolesnikov, Y., & Fedin, K. (2018). Detecting underground cavities using
818 microtremor data: physical modelling and field experiment. *Geophysical*
819 *Prospecting*, 66, 342–353. URL: [https://www.earthdoc.org/content/](https://www.earthdoc.org/content/journals/10.1111/1365-2478.12540)
820 [journals/10.1111/1365-2478.12540](https://www.earthdoc.org/content/journals/10.1111/1365-2478.12540). doi:[https://doi.org/10.1111/](https://doi.org/10.1111/1365-2478.12540)
821 [1365-2478.12540](https://doi.org/10.1111/1365-2478.12540).

822 Leblanc, M., Favreau, G., Tweed, S., Leduc, C., Razack, M., & Mofor, L.
823 (2007). Remote sensing for groundwater modelling in large semiarid areas:
824 Lake chad basin, africa. *Hydrogeology Journal*, 15, 97–100.

825 Lee, E. J., Shin, S. Y., Ko, B. C., & Chang, C. (2016). Early sinkhole detec-

- 826 tion using a drone-based thermal camera and image processing. *Infrared*
827 *Physics & Technology*, 78, 223 – 232. URL: <http://www.sciencedirect.com/science/article/pii/S1350449516303966>. doi:<https://doi.org/10.1016/j.infrared.2016.08.009>.
- 830 Levy, C. R., Burakowski, E., & Richardson, A. D. (2018). Novel measure-
831 ments of fine-scale albedo: Using a commercial quadcopter to measure
832 radiation fluxes. *Remote Sensing*, 10. URL: <https://www.mdpi.com/2072-4292/10/8/1303>. doi:10.3390/rs10081303.
- 834 Lopez, T., Antoine, R., Kerr, Y., Darrozes, J., Rabinowicz, M., Ramillien,
835 G., Cazenave, A., & Genthon, P. (2016). Subsurface hydrology of the lake
836 chad basin from convection modelling and observations. In A. Cazenave,
837 N. Champollion, J. Benveniste, & J. Chen (Eds.), *Remote Sensing and*
838 *Water Resources* (pp. 281–312). Cham: Springer International Publish-
839 ing. URL: https://doi.org/10.1007/978-3-319-32449-4_12. doi:10.
840 1007/978-3-319-32449-4_12.
- 841 Lowe, D. G. (2004). Distinctive image features from scale-invariant keypoints.
842 *International Journal of Computer Vision*, 60, 91–110. URL: <https://doi.org/10.1023/B:VISI.0000029664.99615.94>. doi:10.1023/B:VISI.
843 0000029664.99615.94.
- 845 Majumdar, T. J. (2003). Regional thermal inertia mapping
846 over the indian subcontinent using insat-1d vhr data and its
847 possible geological applications. *International Journal of Re-*

848 *mote Sensing*, 24, 2207–2220. URL: [https://doi.org/10.](https://doi.org/10.1080/01431160210161724)
849 1080/01431160210161724. doi:10.1080/01431160210161724.
850 arXiv:<https://doi.org/10.1080/01431160210161724>.

851 Martnez-Moreno, F., Monteiro Santos, F., Galindo-Zaldvar, J., Gonzalez-
852 Castillo, L., Pedrera, A., Bernando, I., Gonalves, S., & Alves Ribeiro,
853 J. (2018). Characterization of a cave by means of micrograv-
854 ity and electrical resistivity 3d-inversions: Z de braga cave (mira
855 de aire, portugal). *First Break*, 36, 29–34. URL: [https://www.](https://www.earthdoc.org/content/journals/10.3997/1365-2397.2018004)
856 [earthdoc.org/content/journals/10.3997/1365-2397.2018004](https://www.earthdoc.org/content/journals/10.3997/1365-2397.2018004).
857 doi:<https://doi.org/10.3997/1365-2397.2018004>.

858 Mellon, M. T., Jakosky, B. M., Kieffer, H. H., & Christensen, P. R.
859 (2000). High-resolution thermal inertia mapping from the mars
860 global surveyor thermal emission spectrometer. *Icarus*, 148, 437
861 – 455. URL: [http://www.sciencedirect.com/science/article/pii/](http://www.sciencedirect.com/science/article/pii/S0019103500965035)
862 [S0019103500965035](http://www.sciencedirect.com/science/article/pii/S0019103500965035). doi:<https://doi.org/10.1006/icar.2000.6503>.

863 Mochales, T., Casas, A. M., Pueyo, E. L., Pueyo, O., Román, M. T., Pocoví,
864 A., Soriano, M. A., & Ansón, D. (2008). Detection of underground cavi-
865 ties by combining gravity, magnetic and ground penetrating radar surveys:
866 a case study from the zaragoza area, ne spain. *Environmental Geology*,
867 53, 1067–1077. URL: <https://doi.org/10.1007/s00254-007-0733-7>.
868 doi:10.1007/s00254-007-0733-7.

869 Mosciki, W. J. (2006). Temperature anomalies over under-

- 870 ground cavities. *Geophysical Prospecting*, 35, 393–423. URL:
871 [https://onlinelibrary.wiley.com/doi/abs/10.1111/j.1365-2478.](https://onlinelibrary.wiley.com/doi/abs/10.1111/j.1365-2478.1987.tb00825.x)
872 [1987.tb00825.x.](https://onlinelibrary.wiley.com/doi/abs/10.1111/j.1365-2478.1987.tb00825.x) doi:10.1111/j.1365-2478.1987.tb00825.x.
873 arXiv:<https://onlinelibrary.wiley.com/doi/pdf/10.1111/j.1365-2478.1987.tb00825.x>
- 874 Nasipuri, P., Mitra, D., & Majumdar, T. (2005). Generation of ther-
875 mal inertia image over a part of gujarat: A new tool for geolog-
876 ical mapping. *International Journal of Applied Earth Observation*
877 *and Geoinformation*, 7, 129 – 139. URL: [http://www.sciencedirect.](http://www.sciencedirect.com/science/article/pii/S0303243405000358)
878 [com/science/article/pii/S0303243405000358.](http://www.sciencedirect.com/science/article/pii/S0303243405000358) doi:[https://doi.org/](https://doi.org/10.1016/j.jag.2005.02.002)
879 [10.1016/j.jag.2005.02.002.](https://doi.org/10.1016/j.jag.2005.02.002)
- 880 Peters, D. C., Livo, K. E., & Hauff, P. L. (1996). Remote sensing for analysis
881 of mine subsidence and mine wastes. *Environmental Geosciences*, 3, 11–27.
- 882 Putzig, N. E., & Mellon, M. T. (2007). Apparent thermal inertia and
883 the surface heterogeneity of mars. *Icarus*, 191, 68 – 94. URL: [http://](http://www.sciencedirect.com/science/article/pii/S001910350700231X)
884 [www.sciencedirect.com/science/article/pii/S001910350700231X.](http://www.sciencedirect.com/science/article/pii/S001910350700231X)
885 doi:[https://doi.org/10.1016/j.icarus.2007.05.013.](https://doi.org/10.1016/j.icarus.2007.05.013)
- 886 Quinn, A. (1948). *Elements of Photogrammetry*. Syracuse University Press.
887 URL: [https://books.google.fr/books?id=tC07AAAAMAAJ.](https://books.google.fr/books?id=tC07AAAAMAAJ)
- 888 Rahnema, H., Ehsaninezhad, L., Dashti, F., & Talebi, G. (2020). Detection of
889 subterranean cavities and anomalies using multichannel analysis of surface
890 wave. *Geomechanics and Geoengineering*, 0, 1–14. URL: [https://doi.](https://doi.org/10.1016/j.geogeo.2020.01.001)

891 org/10.1080/17486025.2020.1728394. doi:10.1080/17486025.2020.
892 1728394. arXiv:<https://doi.org/10.1080/17486025.2020.1728394>.

893 Rinker, J. (1975). Airborne infrared thermal detection of caves and crevasses.
894 *Photogrammetric engineering and remote sensing*, 44.

895 Ruth, B. E., & Degner, J. D. (1963). Characteristics of sinkhole development
896 and implications for potential cavity collapse. *Measurements*, 11.

897 Sabins, F. F. (2007). *Remote sensing : principles and interpretation*. (3rd
898 ed.). Long Grove, Ill. : Waveland Press. "Reissued 2007 by Waveland
899 Press, Inc."—T.p. verso.

900 SABINS, J., FLOYD F (1969). Thermal Infrared Imagery and Its Application
901 to Structural Mapping in Southern California. *GSA Bulletin*, 80, 397–404.

902 URL: [https://doi.org/10.1130/0016-7606\(1969\)80\[397:TIIAIA\]](https://doi.org/10.1130/0016-7606(1969)80[397:TIIAIA]2.0.CO;2)
903 2.0.CO;2. doi:10.1130/0016-7606(1969)80[397:TIIAIA]2.0.CO;2.

904 arXiv:<https://pubs.geoscienceworld.org/gsabulletin/article-pdf/80/3/397/3432489/>

905 Shul'gin, I., Kleshnin, A., & Verbolova, N. (1958). A photoelectric method for
906 determining the optical properties of plant leaves. *Soviet plant physiology*,
907 *English translation.*) *Fiziol. Rastenii*, 5, 973.

908 Snavey, N., Seitz, S. M., & Szeliski, R. (2008). Modeling the world from
909 internet photo collections. *International Journal of Computer Vision*, 80,

910 189–210. URL: <https://doi.org/10.1007/s11263-007-0107-3>. doi:10.
911 1007/s11263-007-0107-3.

- 912 Turcotte, D. L., & Schubert, G. (2002). *Geodynamics*. (2nd ed.). Cambridge
913 University Press. doi:10.1017/CB09780511807442.
- 914 V. Eppelbaum, L. (2007). Revealing of subterranean karst us-
915 ing modern analysis of potential and quasi-potential fields, .
916 URL: [https://www.earthdoc.org/content/papers/10.3997/](https://www.earthdoc.org/content/papers/10.3997/2214-4609-pdb.179.0797-810)
917 [2214-4609-pdb.179.0797-810](https://www.earthdoc.org/content/papers/10.3997/2214-4609-pdb.179.0797-810). doi:[https://doi.org/10.3997/](https://doi.org/10.3997/2214-4609-pdb.179.0797-810)
918 [2214-4609-pdb.179.0797-810](https://doi.org/10.3997/2214-4609-pdb.179.0797-810).
- 919 Vadillo, I., Benavente, J., Neukum, C., Grtzner, C., Carrasco, F., Az-
920 zam, R., Lin, C., & Reicherter, K. (2012). Surface geophysics and
921 borehole inspection as an aid to characterizing karst voids and vadose
922 ventilation patterns (nerja research site, s. spain). *Journal of Ap-*
923 *plied Geophysics*, *82*, 153 – 162. URL: [http://www.sciencedirect.](http://www.sciencedirect.com/science/article/pii/S0926985112000547)
924 [com/science/article/pii/S0926985112000547](http://www.sciencedirect.com/science/article/pii/S0926985112000547). doi:[https://doi.org/](https://doi.org/10.1016/j.jappgeo.2012.03.006)
925 [10.1016/j.jappgeo.2012.03.006](https://doi.org/10.1016/j.jappgeo.2012.03.006).
- 926 Van Bavel, C., & Hillel, D. (1976). Calculating potential and actual evapo-
927 ration from a bare soil surface by simulation of concurrent flow of water
928 and heat. *Agricultural Meteorology*, *17*, 453–476.
- 929 Vargemezis, G., Tsourlos, P., Fikos, I., Diamanti, N., Angelis, D., & Ama-
930 natidou, E. (2019). Void detection and consolidation filling verification
931 by ert, gpr and seismic refraction methods, . *2019*, 1–5. URL: [https://](https://www.earthdoc.org/content/papers/10.3997/2214-4609.201902525)
932 www.earthdoc.org/content/papers/10.3997/2214-4609.201902525.
933 doi:<https://doi.org/10.3997/2214-4609.201902525>.

- 934 Vasterling, M., & Meyer, U. (2013). Kuenzer c., dech s. (eds) thermal
935 infrared remote sensing. remote sensing and digital image processing.
936 chapter Challenges and Opportunities for UAV-Borne Thermal Imag-
937 ing. (pp. 69–92). Springer, Dordrecht. doi:[https://doi.org/10.1007/
938 978-94-007-6639-6_4](https://doi.org/10.1007/978-94-007-6639-6_4).
- 939 Watson, K. (1973). Periodic heating of a layer over a semi-infinite
940 solid. *Journal of Geophysical Research (1896-1977)*, 78, 5904–
941 5910. URL: [https://agupubs.onlinelibrary.wiley.com/doi/
942 abs/10.1029/JB078i026p05904](https://agupubs.onlinelibrary.wiley.com/doi/abs/10.1029/JB078i026p05904). doi:10.1029/JB078i026p05904.
943 arXiv:<https://agupubs.onlinelibrary.wiley.com/doi/pdf/10.1029/JB078i026p05904>.
- 944 Watson, K. (1975). Geologic applications of thermal infrared images. *Pro-
945 ceedings of the IEEE*, 63, 128–137. doi:10.1109/PROC.1975.9712.
- 946 Whitehead, V. S., Johnson, W. R., & Boatright, J. A. (1986). Vegetation
947 assessment using a combination of visible, near-ir, and thermal-jr avhrr
948 data. *IEEE Transactions on geoscience and remote sensing*, (pp. 107–
949 112).
- 950 Whiteman, C. D., Allwine, K. J., Fritschen, L. J., Orgill, M. M., & Simpson,
951 J. R. (1989). Deep valley radiation and surface energy budget microcli-
952 mates. part i: Radiation. *Journal of Applied Meteorology*, 28, 414–426.
- 953 Wierenga, P. J., Hagan, R. M., & Nielsen, D. R. (1979). Soil
954 temperature profiles during infiltration and redistribution of cool

955 and warm irrigation water. *Water Resources Research*, 6, 230–
956 238. URL: <https://agupubs.onlinelibrary.wiley.com/doi/abs/10.1029/WR006i001p00230>. doi:10.1029/WR006i001p00230.
957 arXiv:<https://agupubs.onlinelibrary.wiley.com/doi/pdf/10.1029/WR006i001p00230>.
958

959 Wynne, J. J., Titus, T. N., & Diaz, G. C. (2008). On developing thermal cave
960 detection techniques for earth, the moon and mars. *Earth and Planetary
961 Science Letters*, 272, 240–250.

962 Yin, D., Chen, S., Li, B., & Guo, W. (2019). Bed separation
963 backfill to reduce surface cracking due to mining under thick
964 and hard conglomerate: a case study. *Royal Society Open
965 Science*, 6, 190880. URL: <https://royalsocietypublishing.org/doi/abs/10.1098/rsos.190880>. doi:10.1098/rsos.190880.
966 arXiv:<https://royalsocietypublishing.org/doi/pdf/10.1098/rsos.190880>.
967

968 Youssef, A. M., El-Kaliouby, H. M., & Zabramawi, Y. A. (2012). In-
969 tegration of remote sensing and electrical resistivity methods in sink-
970 hole investigation in saudi arabia. *Journal of Applied Geophysics*, 87,
971 28 – 39. URL: <http://www.sciencedirect.com/science/article/pii/S0926985112001577>. doi:[https://doi.org/10.1016/j.jappgeo.2012.
972 09.001](https://doi.org/10.1016/j.jappgeo.2012.09.001).
973

974 Youssef, A. M., Zabramwi, Y. A., Gutierrez, F., Bahamil, A. M., Otaibi,
975 Z. A., & Zahrani, A. J. (2020). Sinkholes induced by uncontrolled
976 groundwater withdrawal for agriculture in arid saudi arabia. integra-

977 tion of remote-sensing and geophysical (ert) techniques. *Journal of*
978 *Arid Environments*, 177, 104132. URL: [http://www.sciencedirect.](http://www.sciencedirect.com/science/article/pii/S0140196320300458)
979 [com/science/article/pii/S0140196320300458](http://www.sciencedirect.com/science/article/pii/S0140196320300458). doi:[https://doi.org/](https://doi.org/10.1016/j.jaridenv.2020.104132)
980 [10.1016/j.jaridenv.2020.104132](https://doi.org/10.1016/j.jaridenv.2020.104132).

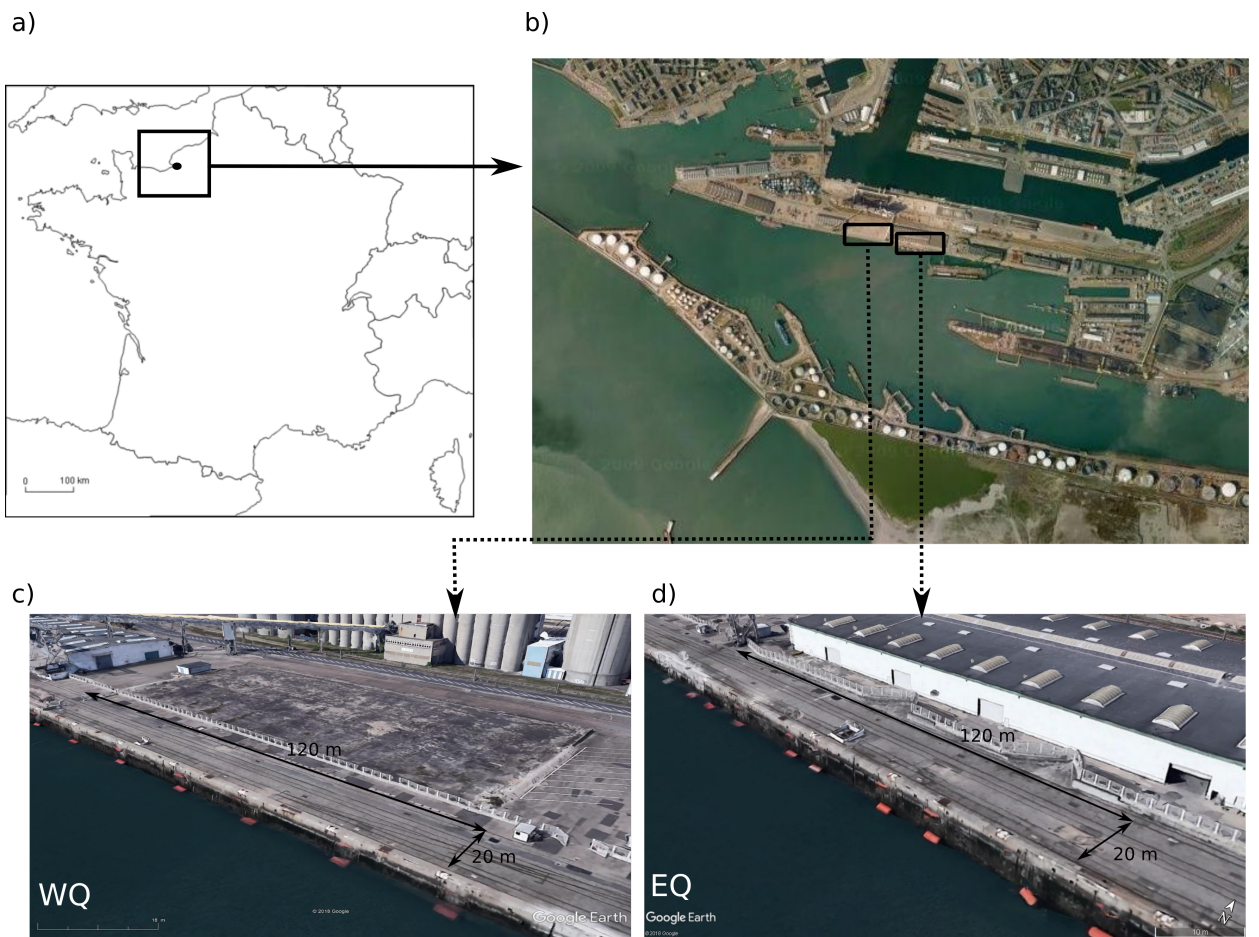


Figure 1: Location of the studied site in Normandy, France.



Figure 2: Photo of typical collapse and deformation observed these last years on the Joannes Couvert quay.

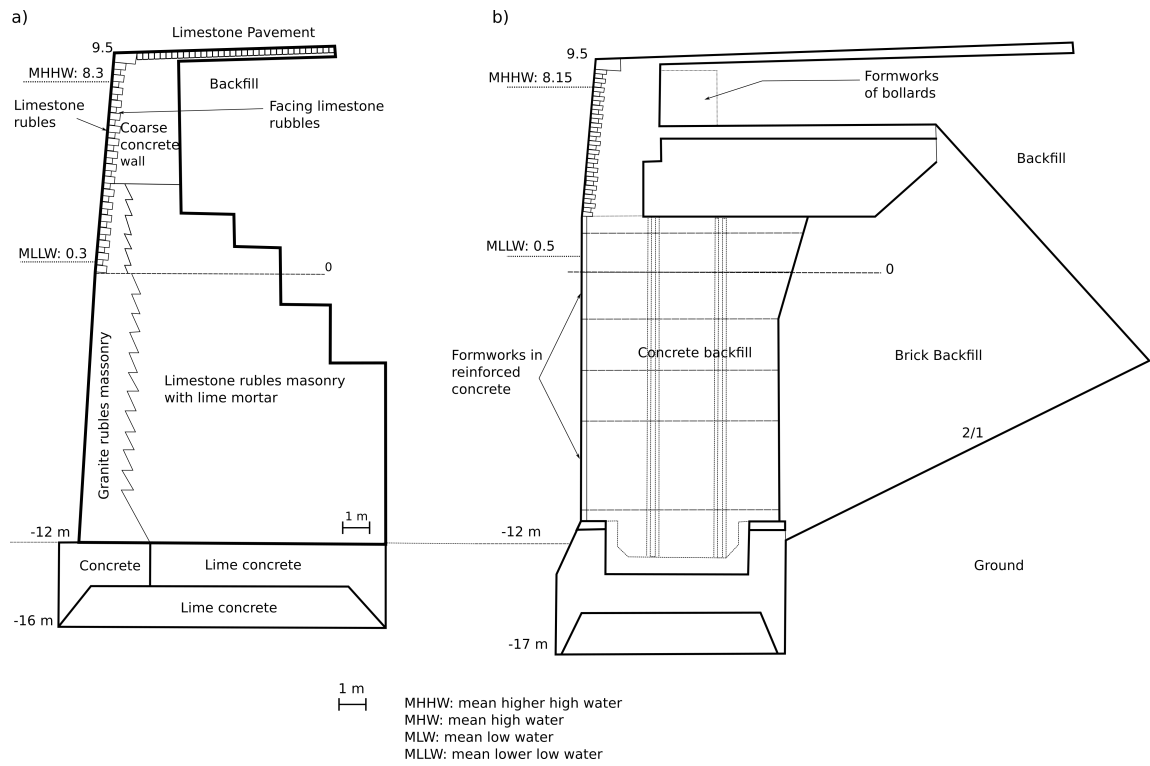


Figure 3: Sketch of internal structure of the quays a) EQ and b) WQ.

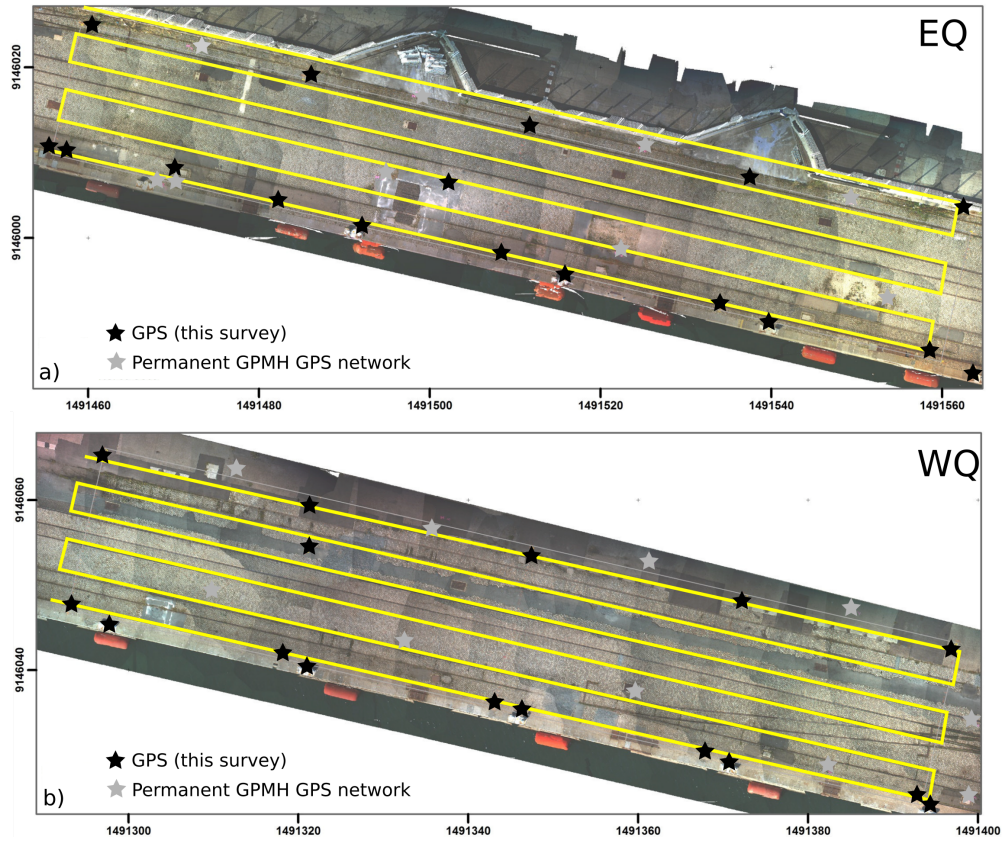


Figure 4: Sketch of the flight plan used during the survey, superimposed with an aerial view of the quays : a) EQ and b) WQ.

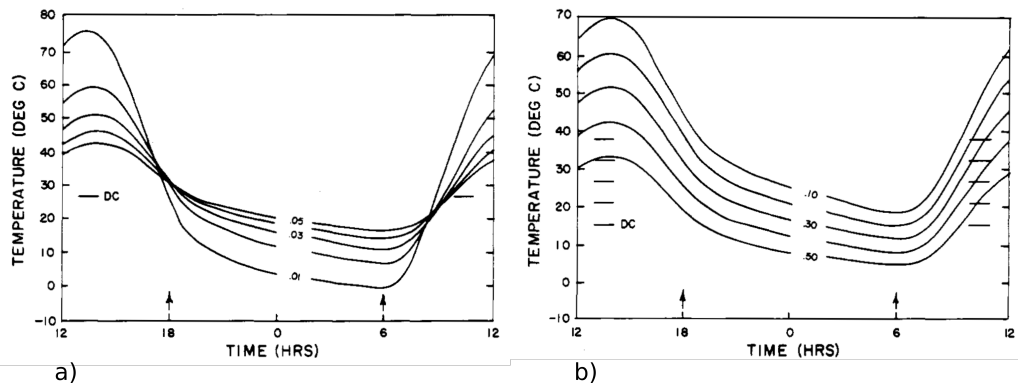


Figure 5: Influence of the thermal inertia and albedo on the surface temperatures (after Watson (1975)).

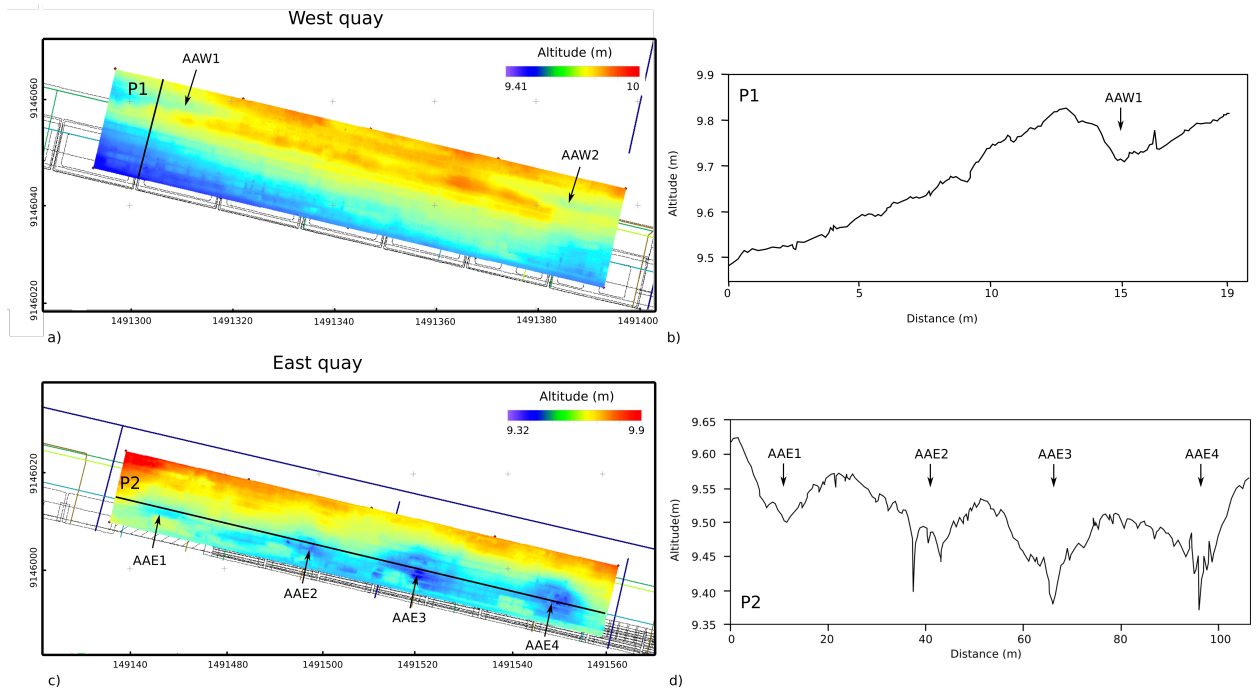


Figure 6: Altimetric maps and measured topographic profiles of a), b) WQ (P1 profile) and c), d) EQ (P2 profile), respectively.

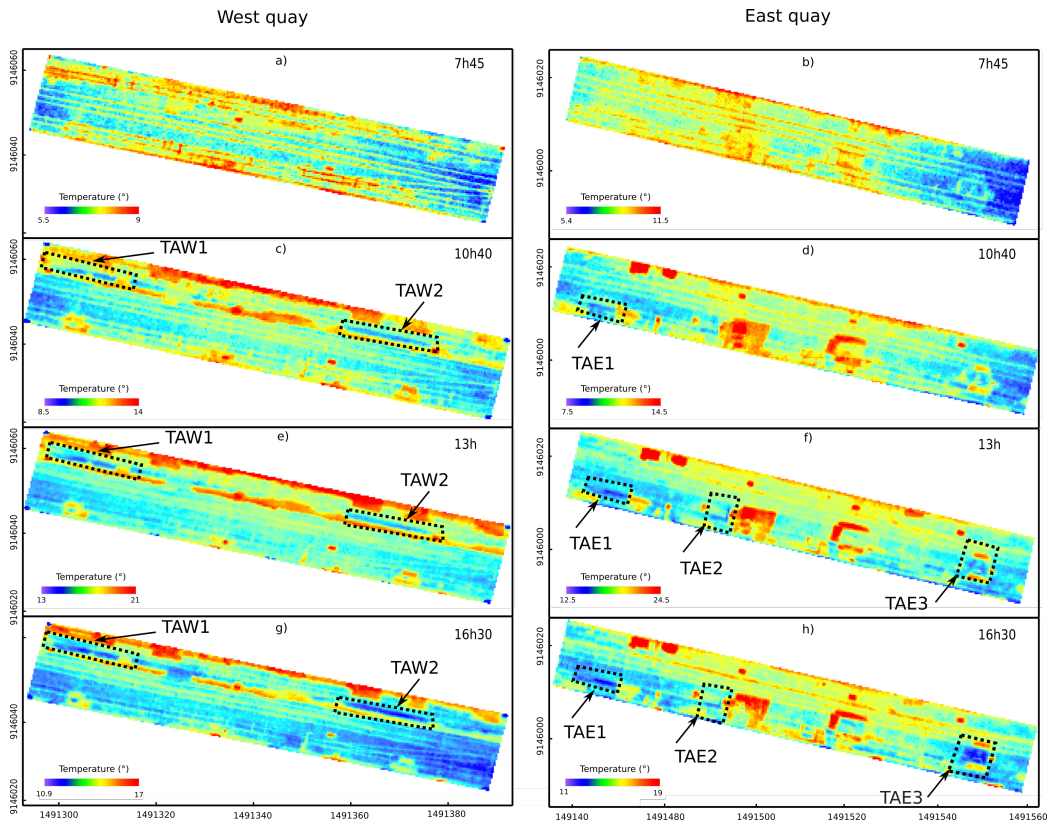


Figure 7: Temperature maps obtained on the WQ and EQ, respectively, during a semi-diurnal cycle.

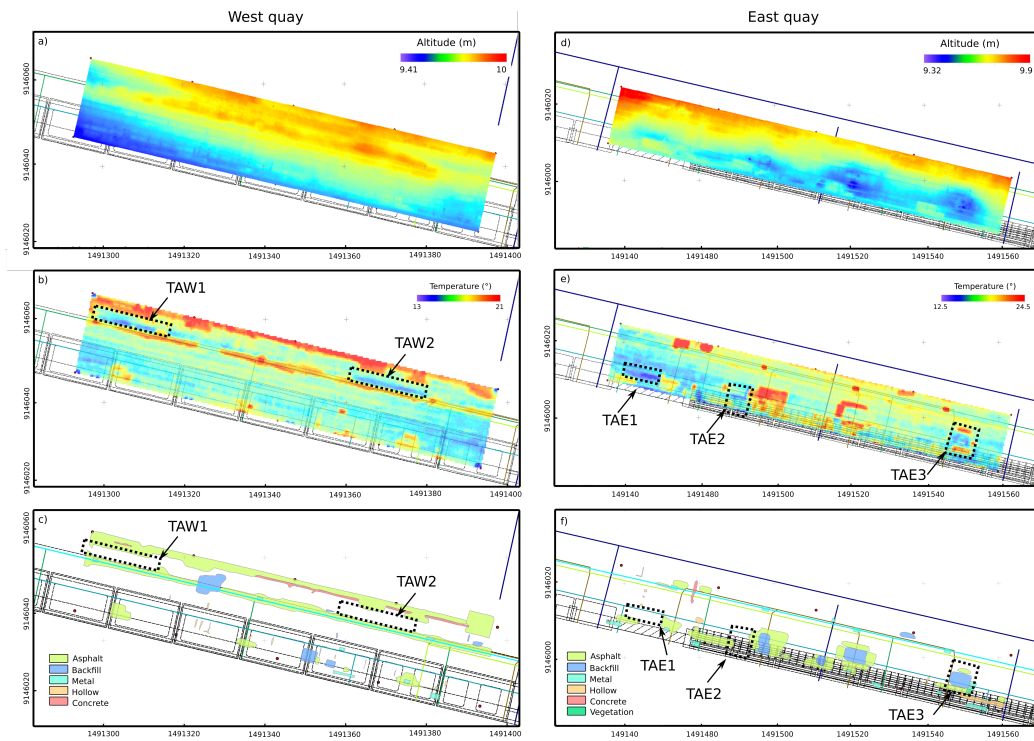


Figure 8: Comparison between a), d) the altimetric map, b), e) the surface temperatures and c), f) the surface indices obtained from visual inspection of the WQ and EQ, respectively. The images are superimposed with a simplified structural map of the quays.

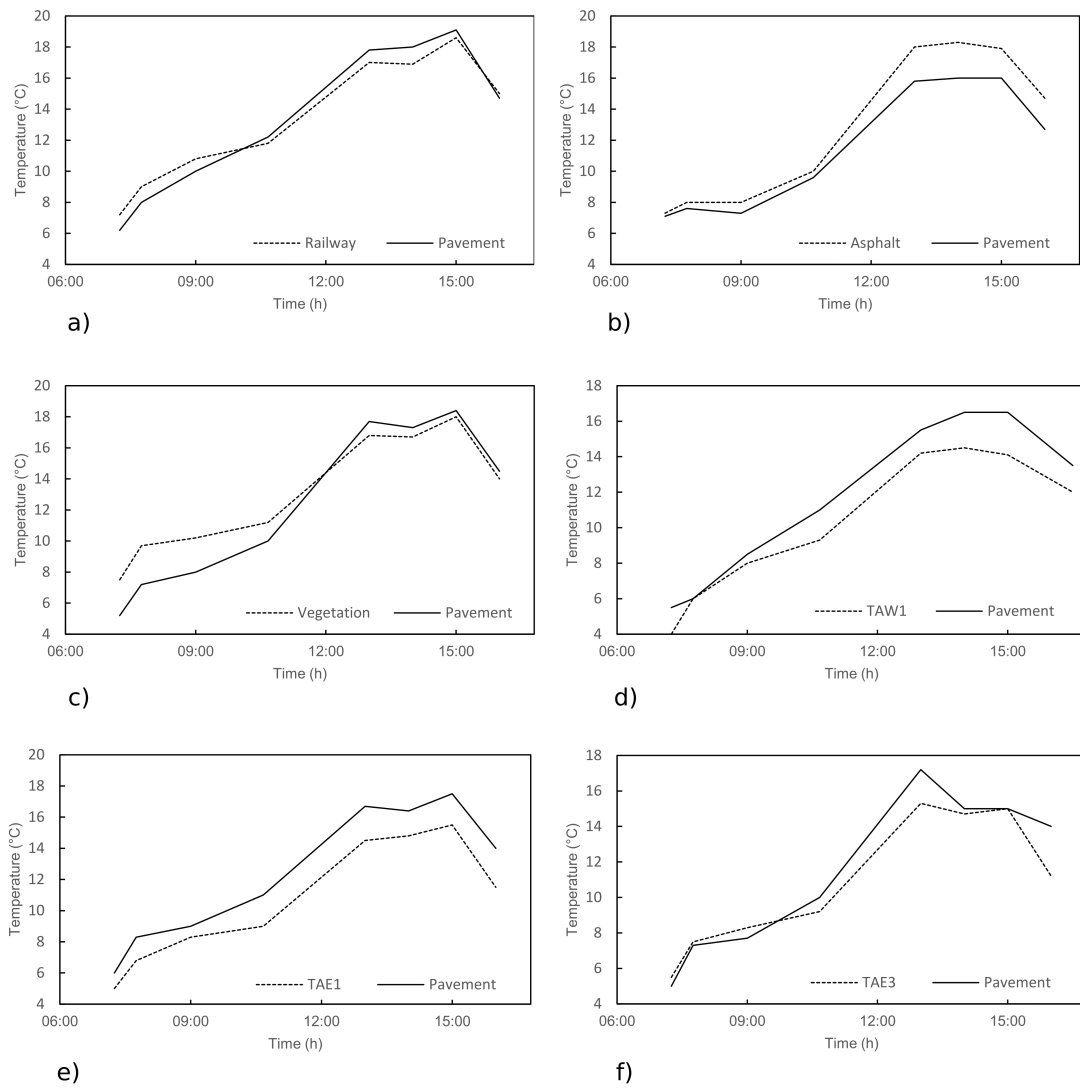


Figure 9: Comparison of temperature evolutions for different materials on the WQ and EQ, illustrating the predominant influence of several parameters/processes on the surface temperature a) thermal inertia (see figure 5a), b) albedo (see figure 5b) and c) impact of the vegetation. Figures d), e) and f) show the temperature evolution of TAW1, TAE1 and TAE3 with their surrounding environment, respectively.

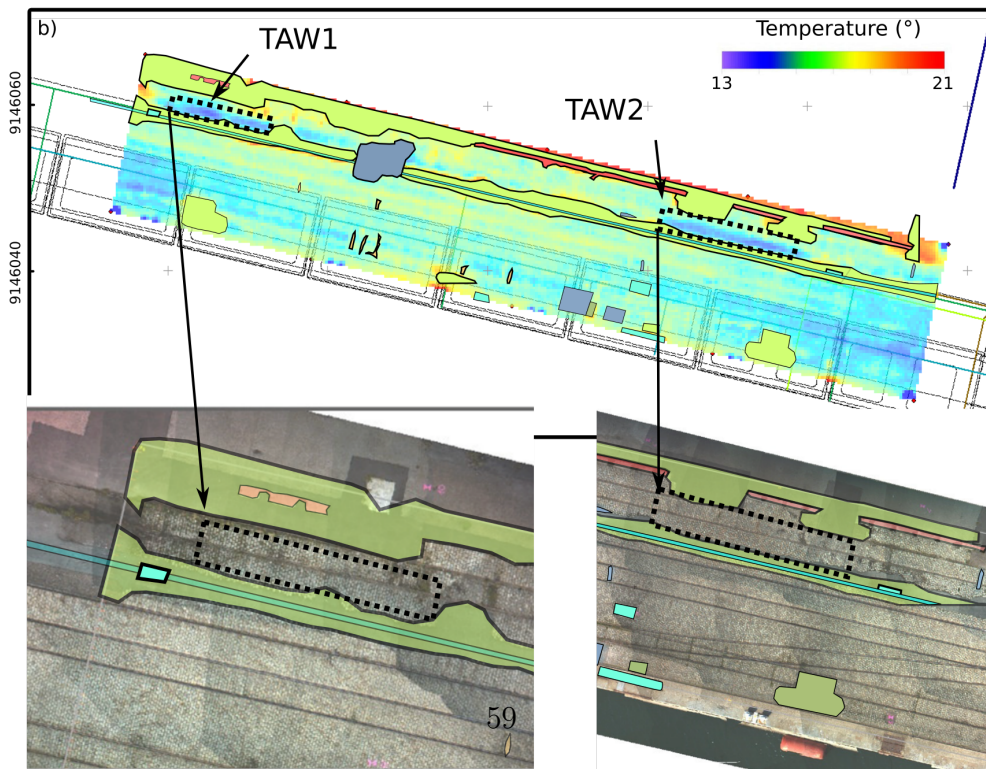
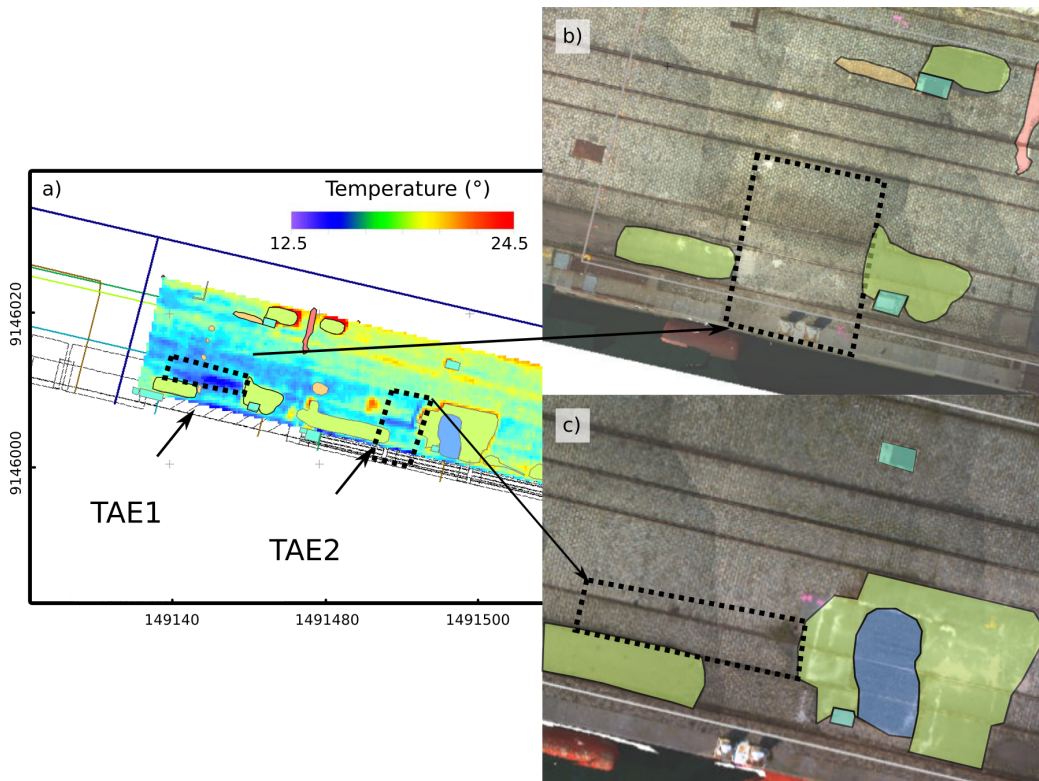


Figure 10: Example of non-correlation between temperature anomalies and albedo.

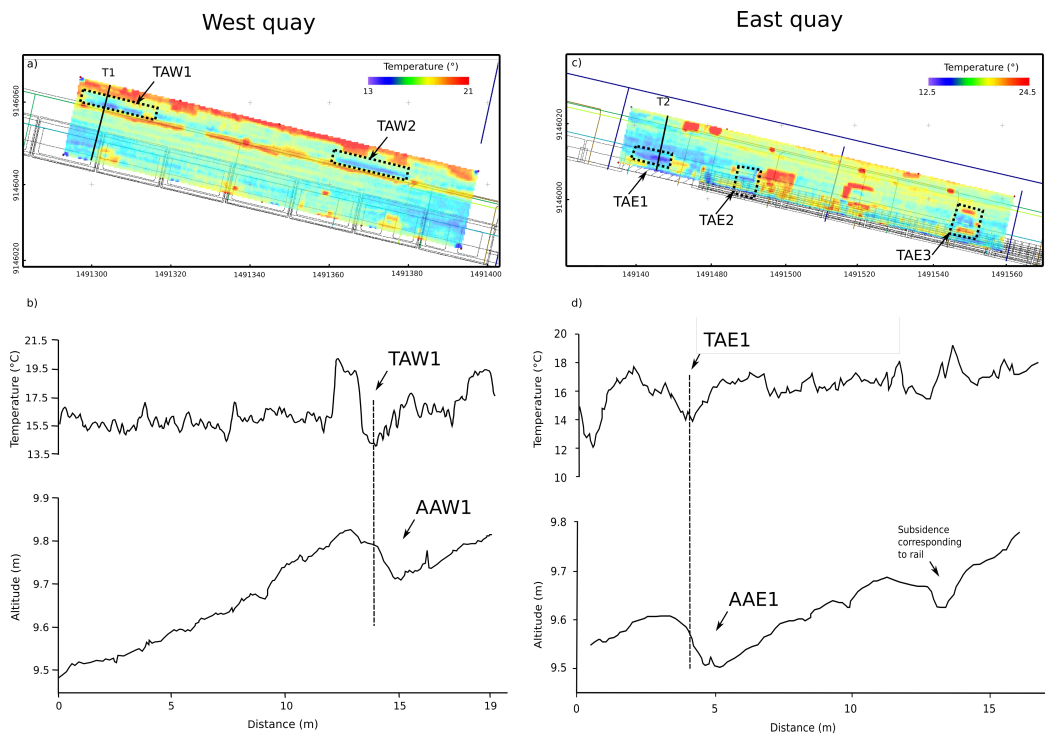


Figure 11: Comparison between the thermal anomaly and the topographic profile for TAW1 (WQ) and TAE1 (EQ).

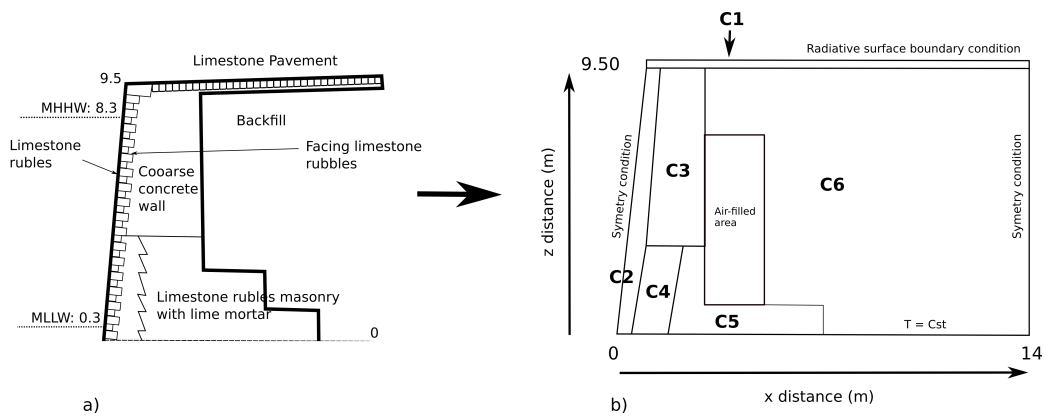


Figure 12: a) Section of the EQ used for the conception of the numerical model and b) Scheme of the thermal model.

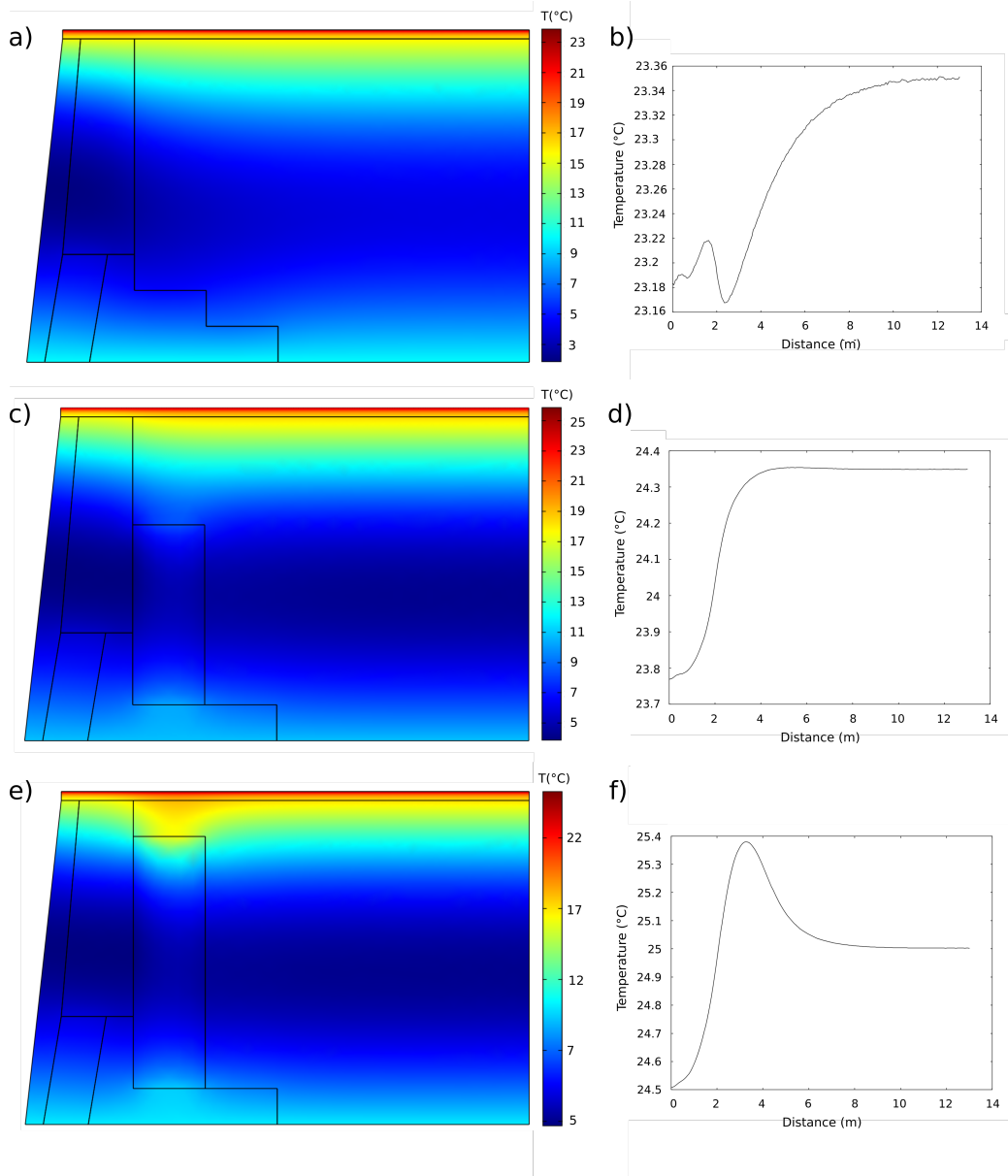


Figure 13: Numerical modelling of the thermal behavior of the EQ a) and b) 2D thermal pattern and surface temperature without cavity; c) and d) 2D thermal pattern and surface temperature for a cavity a 3 m depth; d) and e) 2D thermal pattern and surface temperature for a cavity a 1 m depth.

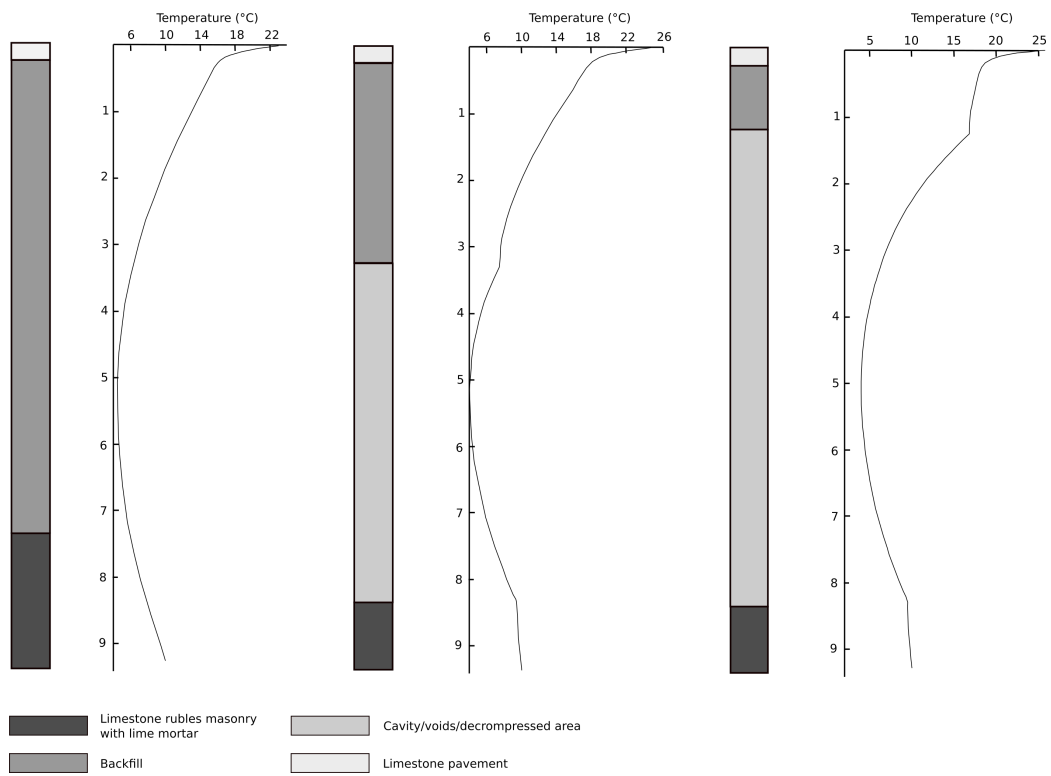


Figure 14: Geological section and corresponding vertical temperature profile for the EQ
a) without cavity, b) for a cavity at 1 m-depth and c) for a cavity at 3 m-depth.

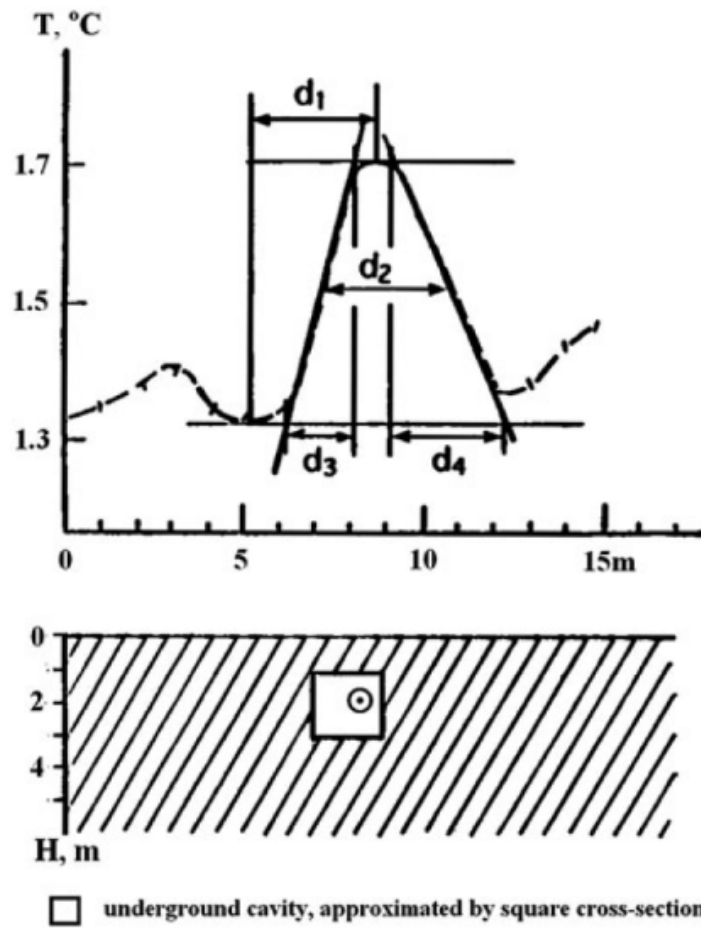


Figure 15: Observed temperature over an underground cavity and geological section taken from Mosciki (2006). The different labels refer to the characteristic distances explained in the author's paper (V. Eppelbaum (2007)).

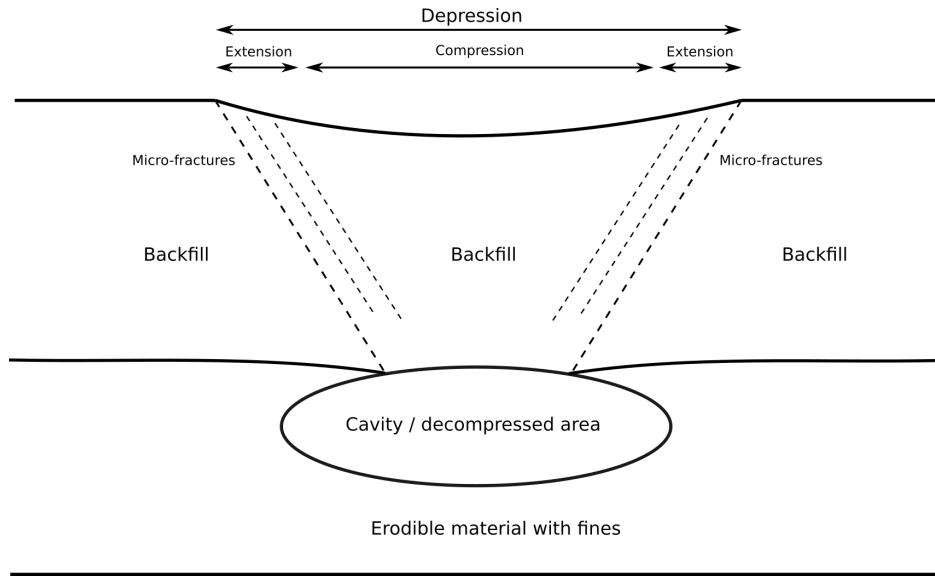


Figure 16: Conceptual model of the mechanical behavior for an homogeneous soil, when surface deformations associated to a subsurface cavity/void are present.

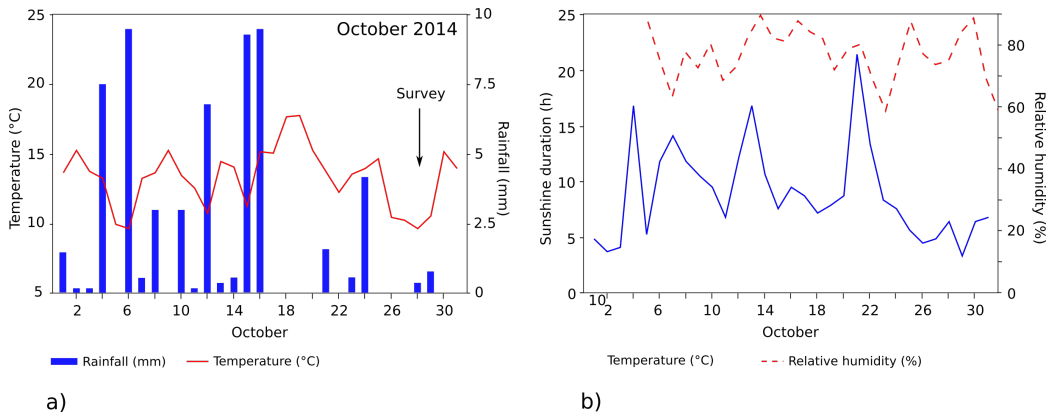


Figure 17: Meteorological data from the Octeville Station, located at 5 km from Le Havre Harbour a) rainfall and mean air temperature and b) sunshine duration and relative humidity.

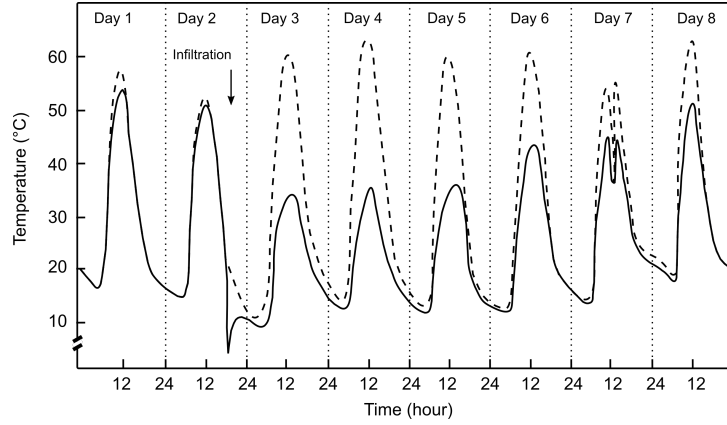


Figure 18: Diurnal variation in soil temperature at the surface of the soil in irrigated (plain line) and nonirrigated (dashed line) soil (after Wierenga et al. (1979)).

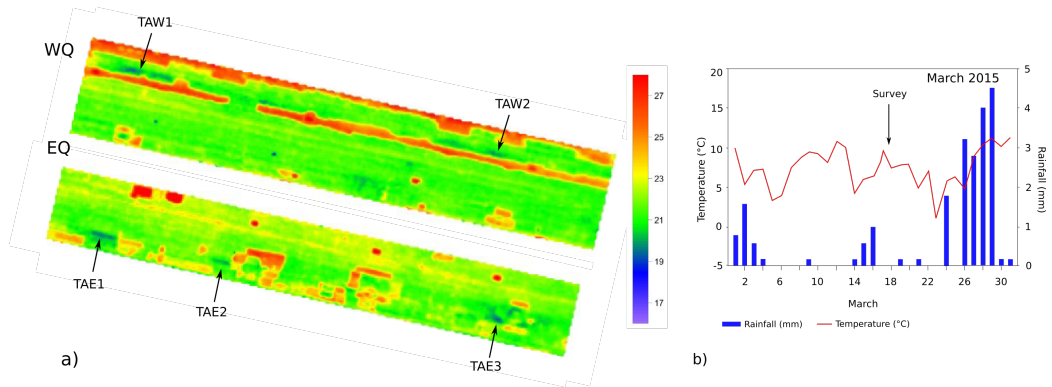


Figure 19: a) Thermal images acquired at 16h on March 17th 2015, showing the same cold anomalies (AAE1 to AAE3, AAW1 and AAW2) present at the same location on the WQ and EQ and b) Precipitations and temperature during March 2015. Note the occurrence of rainfalls just before the survey.